Machine Learning-Enhanced High-Throughput Fabrication and Optimization of Quasi-2D Ruddlesden-Popper Perovskite Solar Cells

Nastaran Meftahi,,† Maciej Adam Surmiak,*,† Sebastian O. Fürer, Kevin James Rietwyk, Jianfeng Lu, Sonia Ruiz Raga, Caria Evans, Monika Michalska, Hao Deng, David P. McMeekin, Tuncay Alan, Dechan Angmo, Doojin Vak, Anthony Chesman, Andrew J. Christofferson, David A. Winkler, Udo Bach, and Salvy P. Russo*

Dr. N. Meftahi, Dr. A. J. Christofferson and Prof. Salvy Russo
ARC Centre of Excellence in Exciton Science, School of Science, RMIT University, Melbourne, Victoria 3001, Australia
E-mail: nastaran.meftahi@rmit.edu.au

Dr. M. A. Surmiak, Dr. S. O. Furer, Dr. K. J. Rietwyk, Dr S. R. Raga, Dr. J. Lu, Ms. M. Michalska, Dr. D. P. McMeekin and Prof. U. Bach
Department of Chemical and Biological Engineering, Monash University, Victoria 3800, Australia
ARC Centre of Excellence for Exciton Science, Monash University, Victoria 3800, Australia
E-mail: adam.surmiak@monash.edu

Dr. D. Angmo, Dr. D. Vak, Dr. A. Chesman and Dr. M. A. Surmiak
CSIRO Manufacturing, Clayton, Victoria 3168, Australia

Dr. J. Lu
State Key Laboratory of Advanced Technology for Materials Synthesis and Processing, Wuhan University of Technology, Wuhan 430070, China

H. Deng, Dr T. Alan
Department of Mechanical and Aerospace Engineering, Faculty of Engineering, Monash University, Clayton, Victoria 3800, Australia

H. Deng
Department of Material Science and Engineering, Monash University, Clayton, Victoria 3800, Australia

Caria Evans
School of Chemistry and Biochemistry, Georgia Institute of Technology, Atlanta, Georgia 30332, United States

Prof. David A. Winkler
Department of Biochemistry and Chemistry, La Trobe Institute for Molecular Science, La Trobe University, Melbourne, Victoria 3086, Australia
School of Pharmacy, University of Nottingham, Nottingham NG7 2RD, United Kingdom

*Corresponding authors
†These authors contributed equally

Keywords: machine learning, quasi 2D Ruddlesden-Popper perovskites, solar cells, high-throughput

Abstract

Organic-inorganic perovskite solar cells (PSCs) are promising candidates for next-generation, inexpensive solar panels due to their high power conversion efficiency, which is on par with their commercial silicon counterparts. However, PSCs suffer from poor stability. A new subset of PSCs, quasi-two-dimensional Ruddlesden-Popper PSCs (quasi-2D RP PSCs), is known for improved photostability and superior resilience to environmental conditions in comparison with three-dimensional (3D) metal-halide PSCs. To expedite the search of new quasi-2D RP PSCs we report a combinatorial, machine learning (ML) enhanced high-throughput perovskite film fabrication and optimization study. We designed a bespoke experiment strategy and produced perovskite films with a range of different compositions through a fully automated drop-casting process. The performance and characterization data of these solar cells were used to train a ML model that allowed for material parameter optimization and directed the design of improved materials. The ML optimized quasi-2D RP perovskite films yielded solar cells with power conversion efficiencies reaching 16.3%.

1. Introduction

Lead halide perovskite solar cells (PSCs) have demonstrated power conversion efficiencies (PCE) up to 25.7%, matching the state-of-the-art silicon solar cells (26.1%).[1] These three-dimensional perovskite materials (ABX_3) typically include a large cation A^+ (for example: $CH_3NH_3^+$, $HC(NH_2)_2^+$ or Cs^+), a smaller cation B^{2+} such as Ge^{2+}, Pb^{2+}, Sn^{2+}, and halide anions X^- (for example: I^-, Br^-, Cl^-).[2-3] The formation of perovskite crystals typically needs to fulfil the Goldschmidt tolerance factor (*GTF*) defined by the equation $GTF = (r_A + r_X)/\sqrt{(r_B + r_X)}$, where r_A, r_B, r_X are the radii of A, B and X ions.[4] A large number of different perovskite materials can be formed based on different permutations of the ionic precursors. Optimization of these precursor ratios has helped to improve the performance as well as stability of these compounds. The latter has to date still proven more challenging due to their sensitivity towards moisture,[5] oxygen,[6] light,[7] temperature[8] and electrical bias,[9] among other factors. Ruddlesden-Popper perovskites (RPPs) are a related material class that has shown some promise to be more resilient to environmental stress then conventional ABX_3 perovskites. In this work, we study RPPs with the general formula $R_2(MA)_{n-1}B_nX_{3n+1}$, where the R^+ stands for a large cation(s) which typically does not satisfy the *GTF* rule, methylammonium cation (MA^+), B^{2+} metal cation, and halide anion (X^-). The quasi-2D structure of RPPs is shown schematically in **Figure 1**. Due to their large size, the R^+ cation cannot be incorporated into the 3D perovskite lattice. Instead, they assemble into layered separated slabs of $[BX_6]^{4-}$ octahedra and intercalated MA^+ cations with a structure similar to the one found in ABX_3 perovskites. The dielectric mismatch of organic and inorganic components creates a favorable environment for the formation of quantum wells and barriers,[10] generating an excellent perovskite for excitonic phenomena.[11-13] Like their 3D counterparts, RPPs have easily tunable band gaps,[14] can be solution-processed,[15] and exhibit high device PCE of ~17-18 %.[16-17]

Crystals of RPPs[18] confer a stability increase by virtue of the hydrophobic aliphatic layers of its alternating structure limiting water ingress,[10, 19] and like 3D PSCs, their properties can be enhanced with a range of perovskite additives.[20] For example, polyvinylpolypyrrolidone (PVP),[21-22] which is widely employed in 3D PSCs, exhibits hydrogen bonding between its carbonyl groups and the protic polar species present in the RPP, leading to the creation of a polymer framework around the crystal structure that furthers enhances stability[23-25] Additionally, the use of different R^+ in the crystal lattice relaxes the *GTF* requirement,[26] resulting in potentially hundreds of thousands of undiscovered, yet highly-performing, compositions.[27-29]

While the RPPs PSC stability is impressive, the current manually fabricated spin-coated devices limit research progress and technology transfer[30-32] because of lack of cross-laboratory standards and reproducibility. The implementation of fully automated and standardized fabrication and measurement techniques[33] would help to significantly improve the comparability of results between different users and different laboratories.[34-35] Most highly efficient lead halide PSCs were fabricated via a spin-coating process, yet a number of alternative fabrication techniques have already been employed, primarily: doctor blading,[36-37] spray,[38-39] ink-jet,[40-41] meniscus printing[42-43] or vacuum deposition.[44-45] These methods require great skill to control and optimize the film crystallization kinetics,[46] precursor rheology[47] and impact on the film quality.[48] This imposes significant financial and time costs on the optimization of fabrication processes required for production of perovskites with a high degree of reproducibility.[49-50] Another factor that slows down the progress is the use of one-step-at-a-time classical systematic experimentation procedure that has a substantial disadvantage of not considering interactions between input parameters.[51] Remarkably, RPP perovskite precursor solutions at molar concentrations (M) below ~0.7 M crystalize into uniform and highly crystalline films when deposited via a simple drop-casting technique.[52-53] An interesting

method was employed in 2021 by Zuo et al.,[54] who used a simple drop casting methodology on mildly preheated substrates for perovskite fabrication. The authors demonstrated that by lowering the concentration of the perovskite precursor solution (< 0.5 M), the solution could spread more evenly across the substrate and form self-assembled, vertically oriented and efficient perovskite films. Extraordinarily, such a simple technique creates new opportunities for rapid compositional screening using drop-cast precursor solutions to form high quality perovskite films. It is known that the reproducibility of PSC fabrication is severely hindered by subtle changes in environmental conditions during deposition,[33] which is likely to impact negatively on the optimization of the fabrication process avoiding this can be accomplished by partial or complete removal of manual handling and human error. In this technique, the mechanism of RPP film formation originates from the precursor solution-substrate surface interactions. Unlike for their 3D counterparts, there are fewer RPP studies focused on crystallization or spread mechanisms (e.g., using additives), controlling the spread and wetting process to ultimately optimize the quality of the resulting RPP film. The drop-casted RPP perovskite film quality depends on a number of factors, such as precursor molarity, substrate temperature and roughness, hydrophilicity or hydrophobicity of the perovskite adjacent charge transporting layer and spread of such precursor, and environmental conditions (pressure, humidity, temperature, atmosphere).[55-56] Given these factors, we focused on the development of an inexpensive, yet highly controllable and rapidly deployable, technique that expands the mechanism of manual perovskite drop-casting to a rapid combinatorial screening. Herein, we describe the automated, machine learning enhanced combinatorial high-throughput (cHTR) screening deposition strategy that allowed for fabrication of multiple new perovskite film compositions via carefully aliquoted, microfluidically[57] prepared precursors. Our bespoke design of experiment (DoE) allows for fabrication of each PSC layer completely free from human intervention. To further accelerate the parameter optimization process, we developed a

state-of-the-art machine learning (ML) protocol from the measurement of electrical and physical properties. This model allows for making predictions on the likely PV properties of RPP films based on a given set of fabrication input parameters. ML algorithms were also used to explore amongst parameters to find the best combinations of permutations in order to develop the device with the highest PV properties.[58-60] To demonstrate our DoE in this work (**Figure 2**) we selected a small sub-set of compositional and fabrication parameters to be varied and only allow a limited number of discrete values which we chose based on our previous knowledge of RPPs.[61] Within this parameter space we then chose a limited number of permutations, fabricated the RP PSCs, and evaluated their photovoltaic performance. These data sets were then analyzed and employed as data to train a machine learning model. The trained model was then used to gain deeper understanding on the influence of specific parameter values on device performance and to predict a parameter set with optimized performance.

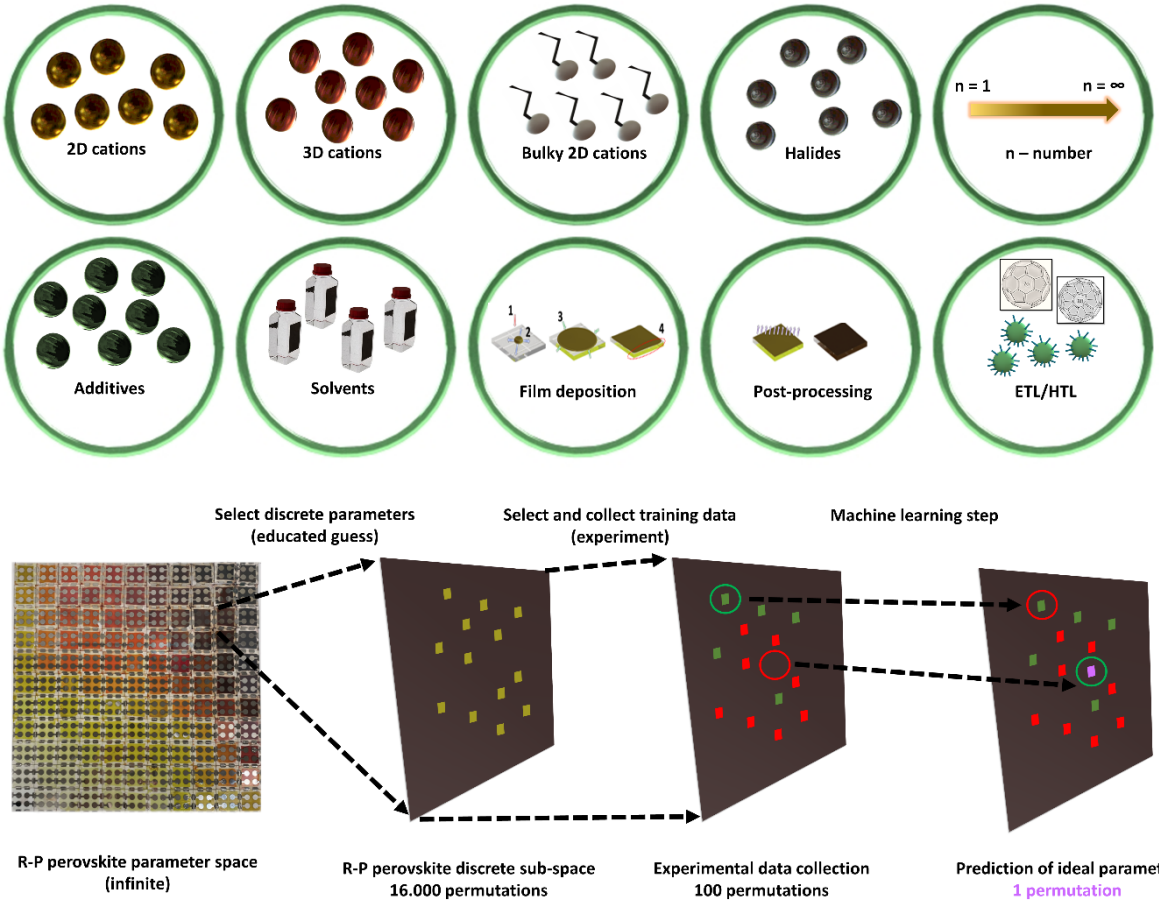

Figure 1. Parameter space for the RPPs. The stoichiometry of RPPs is clearly defined by the formula $R_2(MA)_{n-1}B_nX_{3n+1}$. For each of the components, there is a number of possible candidates which can be mixed in arbitrary ratios, spanning a de-facto infinite compositional parameter space. In a similar way there is a plethora of processing parameters which need to be defined that will ultimately determine the morphology and quality of the resulting perovskite layer and its performance in a photovoltaic device.

This bespoke DoE and the ML model allowed for identification of completely new, improved RPP composition that surpassed the performance of the experimentally chosen champion from the initial subset, yielding to an entirely new champion solar cell with a PCE of ~16.3 % for an active area of 0.1 cm^2.

2. Results and Discussion

2.1 Materials selection

Our DoE began with the selection of the parameter space. The main focus was oriented on generating new quasi-2D RPPs. The variables considered are shown in **Figure 2**. This defines a parameter space with: 10 × 4 × 5 × 5 × 4 × 4 = 16,000 possible permutations. To ensure reproducibility, all the halide salts of 2D and 3D cations were mixed in stoichiometric ratios to obtain the RPP solutions, resulting in films with specified n-numbers, cation, and halide compositions. The drop-casted solutions further contained additives or alternatively were additive-free (denoted as "none"). The temperature of the perovskite annealing step was also varied. This selection permitted for semi-random list of 100 recipes of theoretically high-performing RPPs. See Supplementary Information for further experimental details.

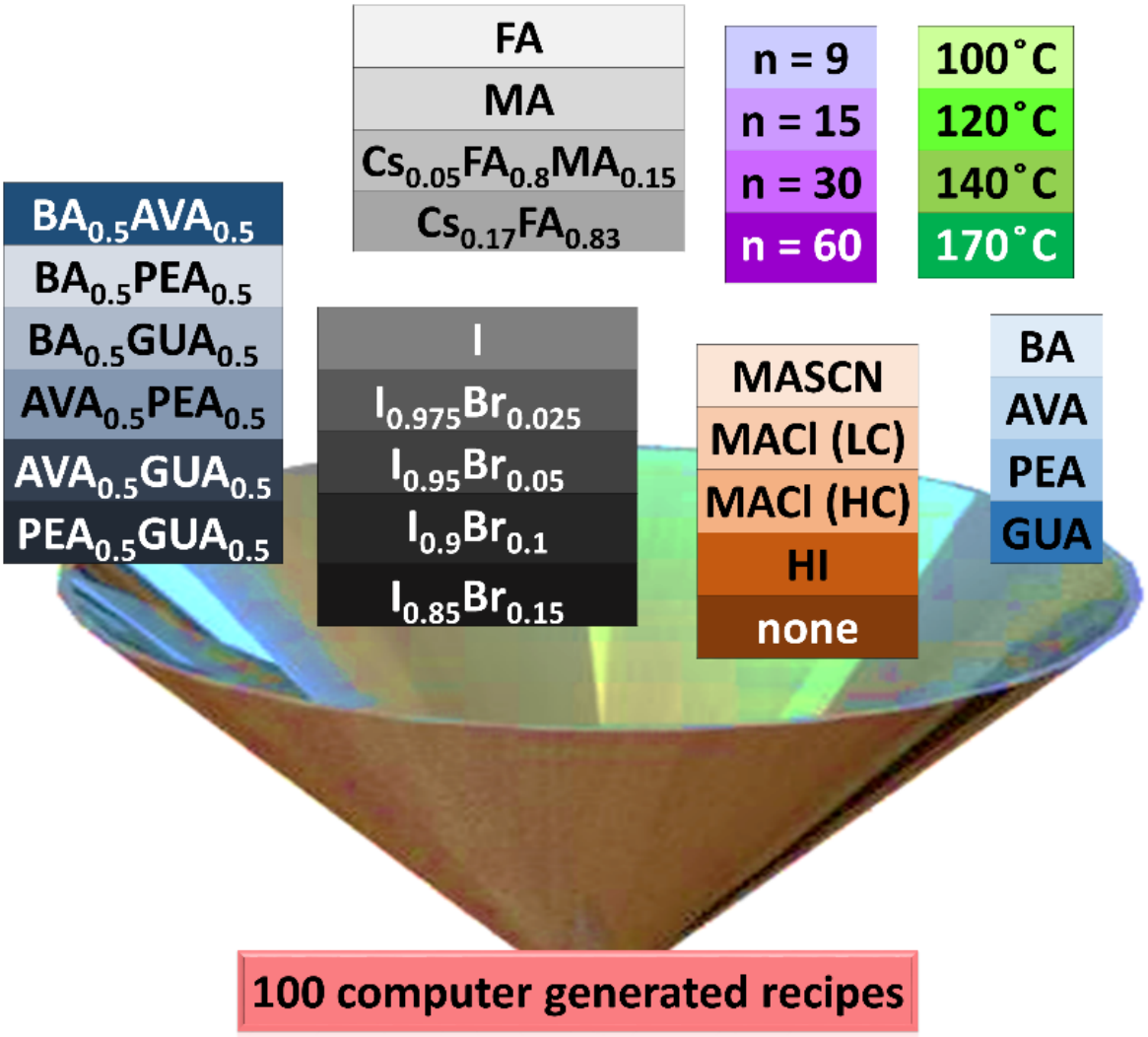

Device	2D cation	3D cation	Halides	Additive options	n-number	Annealing temperature [°C]
1	BA	FA	I0.9Br0.1	HI	15	100
2	BA	Cs0.17FA0.83	I0.975Br0.025	MACl (35%)	15	170
3	BA	MA	I0.85Br0.15	MACl (35%)	9	120
4	BA	FA	I0.975Br0.025	MASCN (5%)	30	100
5	BA	MA	I	None	9	170
6	BA	Cs0.17FA0.83	I0.95Br0.05	MACl (5%)	60	140
7	BA	FA	I0.95Br0.05	HI	60	170
8	BA	Cs0.05FA0.8MA0.15	I	MACl (35%)	30	120
9	BA	Cs0.17FA0.83	I0.9Br0.1	MACl (35%)	30	100
10	BA	Cs0.05FA0.8MA0.15	I0.85Br0.15	MASCN (5%)	9	140
11	AVA	Cs0.17FA0.83	I0.85Br0.15	None	9	100
12	AVA	MA	I0.975Br0.025	MACl (5%)	15	120
13	AVA	FA	I	HI	15	140
14	AVA	Cs0.05FA0.8MA0.15	I0.95Br0.05	MACl (35%)	9	170
15	AVA	Cs0.05FA0.8MA0.15	I0.85Br0.15	MACl (35%)	60	170
16	AVA	FA	I0.95Br0.05	MASCN (5%)	9	100
17	AVA	Cs0.05FA0.8MA0.15	I	HI	60	140
18	AVA	Cs0.17FA0.83	I0.9Br0.1	MASCN (5%)	30	120
19	AVA	Cs0.17FA0.83	I0.9Br0.1	MACl (35%)	60	170
20	AVA	MA	I0.975Br0.025	None	30	140
21	PEA	MA	I0.95Br0.05	MACl (5%)	30	100
22	PEA	FA	I	MACl (35%)	9	120
23	PEA	FA	I0.975Br0.025	MACl (5%)	60	100
24	PEA	MA	I0.85Br0.15	MACl (35%)	60	140
25	PEA	Cs0.05FA0.8MA0.15	I0.95Br0.05	None	15	140
26	PEA	MA	I0.85Br0.15	None	15	120
27	PEA	Cs0.05FA0.8MA0.15	I0.975Br0.025	MASCN (5%)	9	120
28	PEA	Cs0.17FA0.83	I	MACl (35%)	15	170
29	PEA	Cs0.05FA0.8MA0.15	I0.9Br0.1	HI	30	140
30	PEA	Cs0.17FA0.83	I0.9Br0.1	MACl (35%)	60	170
31	GUA	Cs0.05FA0.8MA0.15	I	MACl (35%)	30	120
32	GUA	MA	I0.85Br0.15	MACl (5%)	9	100
33	GUA	Cs0.17FA0.83	I0.975Br0.025	MACl (35%)	30	170
34	GUA	FA	I0.85Br0.15	MASCN (5%)	15	100
35	GUA	Cs0.05FA0.8MA0.15	I0.95Br0.05	MACl (5%)	9	120
36	GUA	FA	I0.9Br0.1	MACl (35%)	15	140
37	GUA	FA	I0.975Br0.025	MACl (35%)	60	140
38	GUA	Cs0.17FA0.83	I0.95Br0.05	HI	15	140
39	GUA	Cs0.05FA0.8MA0.15	I0.9Br0.1	None	30	170
40	GUA	MA	I	MASCN (5%)	60	170
41	BA:AVA	MA	I0.975Br0.025	MACl (5%)	30	120
42	BA:AVA	Cs0.17FA0.83	I	MACl (35%)	60	170
43	BA:AVA	FA	I0.95Br0.05	MASCN (5%)	9	120
44	BA:AVA	FA	I0.85Br0.15	MASCN (5%)	9	100
45	BA:AVA	Cs0.17FA0.83	I0.85Br0.15	MACl (35%)	30	140
46	BA:AVA	Cs0.05FA0.8MA0.15	I	None	60	140
47	BA:AVA	MA	I0.9Br0.1	HI	9	100
48	BA:AVA	Cs0.05FA0.8MA0.15	I0.975Br0.025	MACl (35%)	15	120
49	BA:AVA	Cs0.17FA0.83	I0.9Br0.1	MACl (35%)	15	140

Device	2D cation	3D cation	Halides	Additive options	n-number	Annealing temperature [°C]
50	BA:AVA	Cs0.05FA0.8MA0.15	I0.95Br0.05	MACl (5%)	15	170
51	BA:PEA	Cs0.05FA0.8MA0.15	I	MACl (35%)	60	120
52	BA:PEA	Cs0.05FA0.8MA0.15	I0.9Br0.1	MACl (5%)	9	100
53	BA:PEA	Cs0.17FA0.83	I0.85Br0.15	MACl (35%)	15	170
54	BA:PEA	FA	I0.95Br0.05	MASCN (5%)	15	140
55	BA:PEA	Cs0.17FA0.83	I0.95Br0.05	HI	30	120
56	BA:PEA	MA	I0.975Br0.025	MACl (35%)	15	170
57	BA:PEA	Cs0.05FA0.8MA0.15	I0.9Br0.1	MACl (35%)	9	140
58	BA:PEA	FA	I	None	60	100
59	BA:PEA	MA	I0.975Br0.025	HI	30	120
60	BA:PEA	Cs0.17FA0.83	I0.85Br0.15	None	60	100
61	BA:GUA	FA	I0.95Br0.05	MACl (5%)	9	170
62	BA:GUA	Cs0.05FA0.8MA0.15	I0.975Br0.025	None	30	100
63	BA:GUA	MA	I0.85Br0.15	MACl (35%)	15	120
64	BA:GUA	MA	I0.9Br0.1	None	9	100
65	BA:GUA	FA	I	MASCN (5%)	30	170
66	BA:GUA	Cs0.17FA0.83	I0.975Br0.025	HI	60	140
67	BA:GUA	MA	I	MACl (35%)	15	120
68	BA:GUA	Cs0.17FA0.83	I0.95Br0.05	HI	15	140
69	BA:GUA	FA	I0.85Br0.15	MACl (5%)	60	120
70	BA:GUA	Cs0.05FA0.8MA0.15	I0.9Br0.1	MACl (35%)	9	100
71	AVA:PEA	Cs0.17FA0.83	I0.95Br0.05	None	15	100
72	AVA:PEA	MA	I0.85Br0.15	MASCN (5%)	30	170
73	AVA:PEA	FA	I	MACl (5%)	9	170
74	AVA:PEA	Cs0.05FA0.8MA0.15	I	MACl (35%)	60	140
75	AVA:PEA	MA	I0.975Br0.025	HI	15	120
76	AVA:PEA	Cs0.17FA0.83	I0.9Br0.1	MACl (35%)	30	120
77	AVA:PEA	MA	I0.85Br0.15	MACl (35%)	30	100
78	AVA:PEA	FA	I0.9Br0.1	MACl (5%)	9	140
79	AVA:PEA	Cs0.05FA0.8MA0.15	I0.975Br0.025	MASCN (5%)	60	100
80	AVA:PEA	Cs0.17FA0.83	I0.95Br0.05	HI	60	170
81	AVA:GUA	FA	I0.975Br0.025	None	15	120
82	AVA:GUA	MA	I0.85Br0.15	MASCN (5%)	9	140
83	AVA:GUA	Cs0.17FA0.83	I0.9Br0.1	MASCN (5%)	60	120
84	AVA:GUA	MA	I0.85Br0.15	None	30	170
85	AVA:GUA	Cs0.05FA0.8MA0.15	I0.95Br0.05	MACl (5%)	60	170
86	AVA:GUA	Cs0.05FA0.8MA0.15	I0.975Br0.025	HI	9	100
87	AVA:GUA	Cs0.17FA0.83	I	MACl (5%)	30	140
88	AVA:GUA	FA	I0.95Br0.05	MACl (35%)	15	100
89	AVA:GUA	MA	I	MACl (35%)	30	170
90	AVA:GUA	FA	I0.9Br0.1	HI	60	120
91	PEA:GUA	Cs0.05FA0.8MA0.15	I0.95Br0.05	MASCN (5%)	30	100
92	PEA:GUA	Cs0.17FA0.83	I	None	30	140
93	PEA:GUA	MA	I0.9Br0.1	MACl (35%)	60	100
94	PEA:GUA	Cs0.17FA0.83	I0.9Br0.1	MACl (5%)	9	140
95	PEA:GUA	FA	I	MACl (5%)	15	170
96	PEA:GUA	FA	I0.85Br0.15	HI	60	120
97	PEA:GUA	MA	I0.85Br0.15	MACl (35%)	30	100
98	PEA:GUA	Cs0.05FA0.8MA0.15	I0.975Br0.025	None	9	120
99	PEA:GUA	MA	I0.95Br0.05	MASCN (5%)	9	170
100	PEA:GUA	FA	I0.975Br0.025	MACl (35%)	15	140

Figure 2. Experimental parameter space explored in this study. All halide salts, cations and additives were mixed to ensure the same stoichiometric ratios and to obtain the desired n-numbers. All other fabrication parameters were fixed. Abbreviations: BA is butylammonium, AVA is 5-amminovaleric acid, PEA is phentylammonium, GUA is guanidinium, FA is formamidinium, MA is methylammonium, I is iodide, Br is bromide, MASCN is methylammonium thiocyanate, MACl is methylammonium chloride (where LC is low concentration and HC is high concentration), HI is iodic acid, and None stands for equivalent pure solvent used for dissolving the rest of additives. The RPP film post-annealing was also a varied parameter as denoted.

2.2 Automated solar cell fabrication

Importantly, we demonstrate a new, easily adaptable cHTR deposition system that allows for the rapid combinatorial screening of quasi-2D RPPs. We tracked all experimental deposition conditions and parameters to serve as an additional productivity measure and reproducibility check **(Supporting Information)**. This high-throughput system employed pre-cut and pre-patterned substrate reported by us earlier,[56] along with a microfluidic precursor solution agitating and dosing system. The substrates were thoroughly cleaned and then automatically

coated with NiO following the previously reported method[62] (see Supplementary Information for exact fabrication details). By accurately controlling the precursor aliquots via pre-defined strokes of programmable syringe pump (Chemyx 4000), we were able to quickly and accurately fabricate any given perovskite system. In short, the proposed cHTR system allows us to mitigate the impact of human-induced error, thus improving the lab-to-lab and user-to-user reproducibility. This systematic automated DoE is a promising step towards fully unbiased, rapid exploration and population of vast compositional spaces in order to streamline the generation of a large and widely accessible perovskite libraries of unforeseen quality. After the perovskite deposition, a multi-step evaporation process was employed to assure reproducibility and uniformity of the devices. Finally, we fabricated 600 individual solar cells following the proposed recipes, and then proceeded with the data extraction through the automated electrical characterization[62] (see Supporting Information for more details) whilst ensuring that the only possible difference in the results would originate from RPPs films.

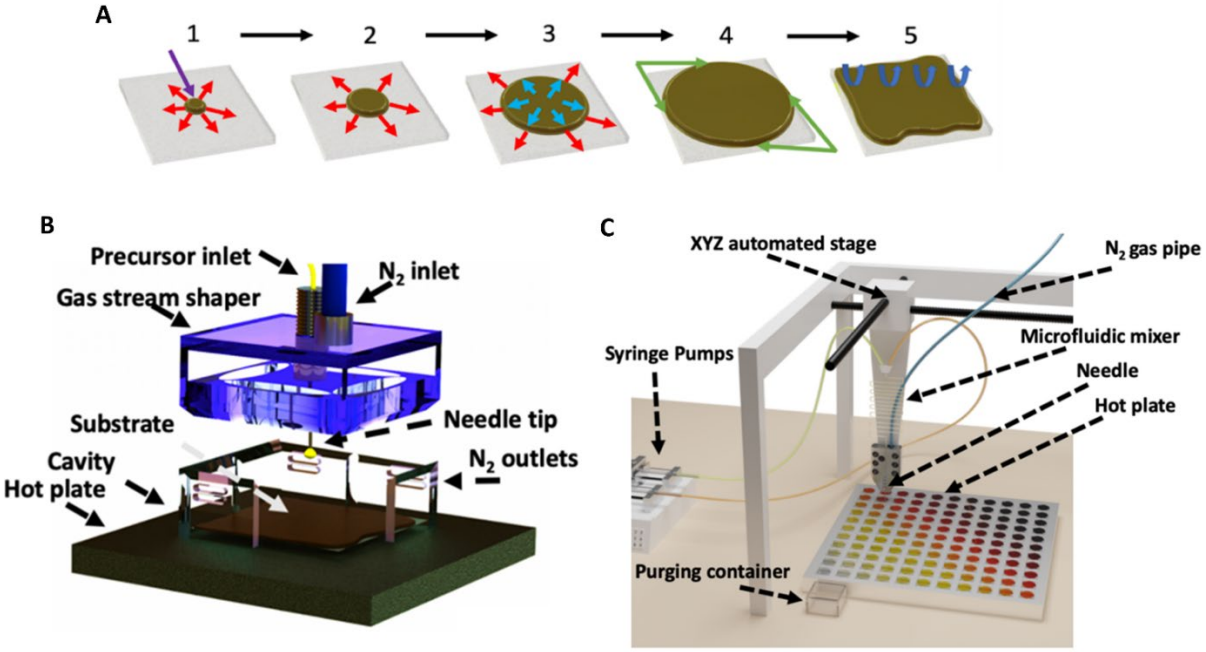

Figure 3. The combinatorial high-throughput spin-coating free perovskite film deposition system. For quasi-2D RPP systems. A) The conceptual view of the key components and working principle of the solution agitating and deposition system. The deposition head with blunt needle inside of the 3D printed crystallization cavity. B) The spreading and crystallization mechanism: (1) syringe pump stroke pushes the droplet onto the substrate; (2) isotropic movement distributes precursor solution across the substrate; (3) precursor surface tension reaches the edge; (4) causing the van der Waals surface tension to break and the solution to spread along the edge; (5) solvent evaporation and timely application of N_2 quenching gas causes film formation. See the Supplementary Information more details.

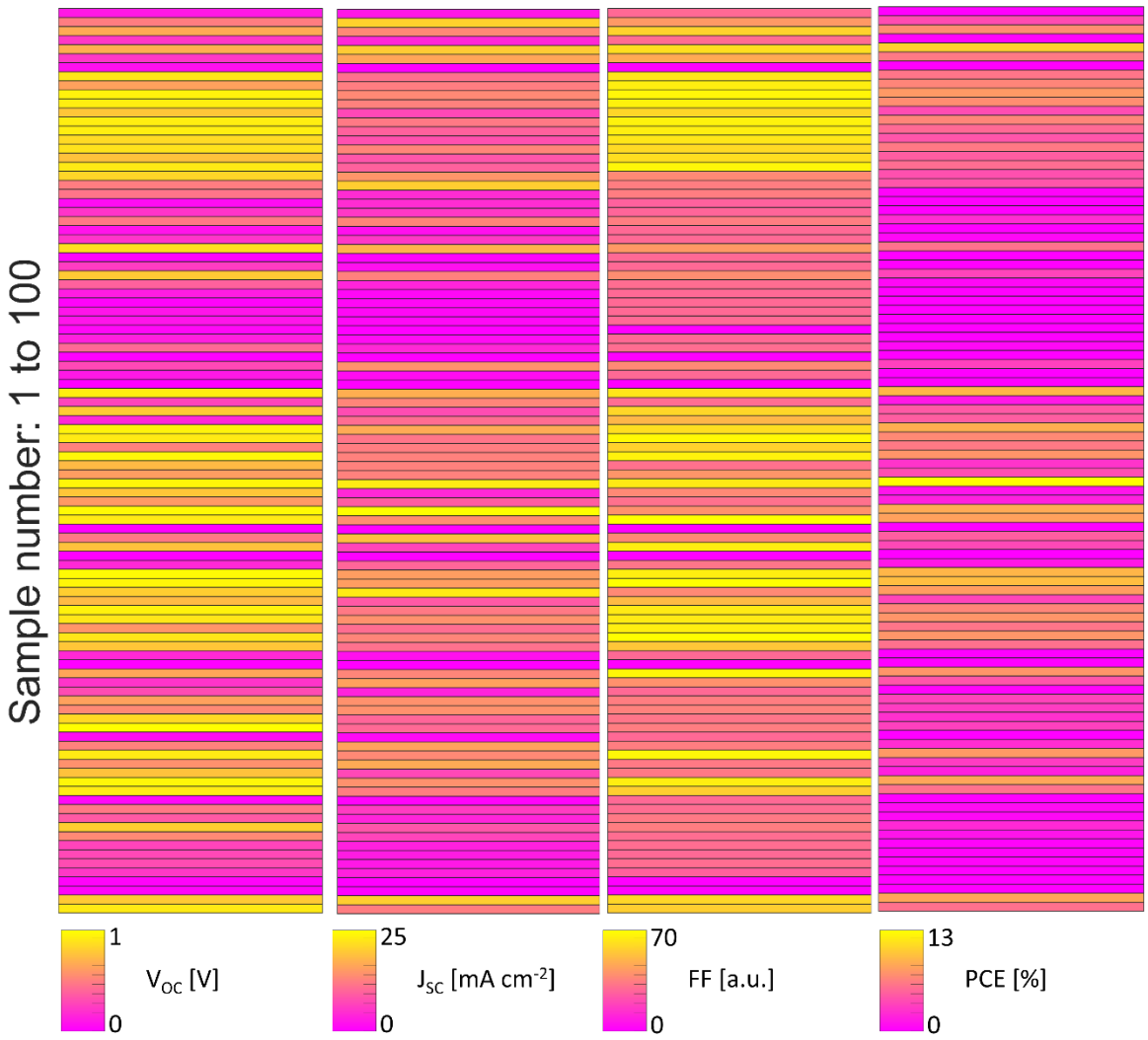

Figure 4. The first screening results. More detailed photovoltaic data can be sound in SI.

2.3 Machine learning optimized recipe

In this project, we used ML algorithms to investigate the effect and contribution of each fabrication permutation on PV properties such as PCE, open circuit voltage (V_{OC}), short circuit current density (J_{SC}) and fill factor (FF). More material details can be found in Supporting Information. We used the 100 experimentally developed devices as described in section 2.1 as our dataset. These device recipes were generated by randomly applying preselected parameters such as: 2D cations (n-BA1, AVA1, PEA1, GUA1, nBA0.5AVA0.5, nBA0.50PEA0.5, n-BA0.5GUA0.5, AVA0.5PEA0.5, AVA0.5GUA0.5, PEA0.5GUA0.5), 3D cations (FA, MA, Cs0.05FA0.8MA0.15, Cs0.17FA0.83), halides (I, I0.975Br0.025, I0.95Br0.05, I0.85Br0.15, I0.9Br0.1), additive options (MASCN, 5% MACl, 35% MACl, , HI, no additive), n-number options (9, 15, 30, 60) and annealing temperature [°C] (100, 120, 140 and 170). As described above, all possible combinations of these device parameters would require the experimental

development and testing of 16,000 different devices. We therefore employed machine learning on a subset of fabrication parameters to find the optimum fabrication parameters which result in maximum performance, which we define as the champion recipe. Generally, ML models describe a quantitative relationship between the structure of compounds and a specific property. Here, we instead used ML techniques to explore the quantitative relationships between the device fabrication parameters and the photovoltaic performance parameters (PCE, V_{OC}, J_{SC} and FF) of the resulting solar cell devices. To the best of our knowledge, this is the first reported study that employs ML optimization combined with automated fabrication process to design PSCs. We used the MLREM (Multiple Linear Regression with Expectation Maximization) algorithm[63] implemented in the CSIRO-BioModeller® package.[64-66] In general, ML models require descriptors (mathematical entities that encode physical or chemical properties) to find relationships between descriptors and the target property. In our dataset, the majority of data points (RPP PSCs) had the same chemical components, so molecular descriptors were not required. Thus, we used the list of fabrication parameters for devices (**Figure 3)** as descriptors to build the models. In our DoE we used 1-hot binary descriptors (i.e., 1 if feature is present and 0 if absent) for fabrication parameters such as: 3D-cations, halides, additive options, n-number of option and annealing temperature.

The MLREM algorithm is a very sparse feature selection method that removes less relevant descriptors in a context-dependent way and optimizes the balance between the variance (model complexity) and bias (model simplicity). The Laplacian prior method is used to give zero weight to irrelevant descriptors and automatically remove them from the model. This feature selection algorithm is similar to the LASSO technique, and is based on L1 regression.[67-68] In a general machine learning modeling procedure, the dataset would be divided into a training set (e.g., 80% of dataset) to generate the model and a test set (e.g., 20% of the dataset) to evaluate the predictive power of the model. In this study, our aim was mainly focused on investigating the contribution of fabrication parameters on PCE, V_{OC}, J_{SC} and FF rather than developing a model for property prediction purposes. Therefore, we derived the models by applying 100% of data as training set to elucidate the contribution of the variables listed in Figure only on PCE, V_{OC}, J_{SC} and FF. This information then provided guidance on how to fabricate new and more efficient RPP PSCs. The performance of MLREM models were assessed by the R^2 statistics (squared correlation coefficient), and the standard error of estimation (SEE).[69-70] **Table 1** shows the statistics of MLREM models for PCE, V_{OC}, J_{SC}, and FF. These results indicate the significant parameters (descriptors) for each property. **Figure 5** shows the contribution as well as the effect of descriptors on each property where the parameters with positive and negative

sign increase and decrease the values of property, respectively.

Table 1. Statistics of MLREM models of PCE (%), V_{OC} (V), J_{SC} (mA cm^{-2}), and FF applying 100% of dataset as training set. N_{eff} is the number of effective parameters (weights) and N_{desc} is the final number of parameters in the models. SEE is the scaled standard error of estimation.

Training Set	N_{desc}	N_{eff}	R^2	SEE
PCE [%]	33	34	0.54	0.21
V_{OC} [V]	33	34	0.54	0.28
J_{SC} [mA cm^{-2}]	33	34	0.50	0.22
FF	33	34	0.53	0.23

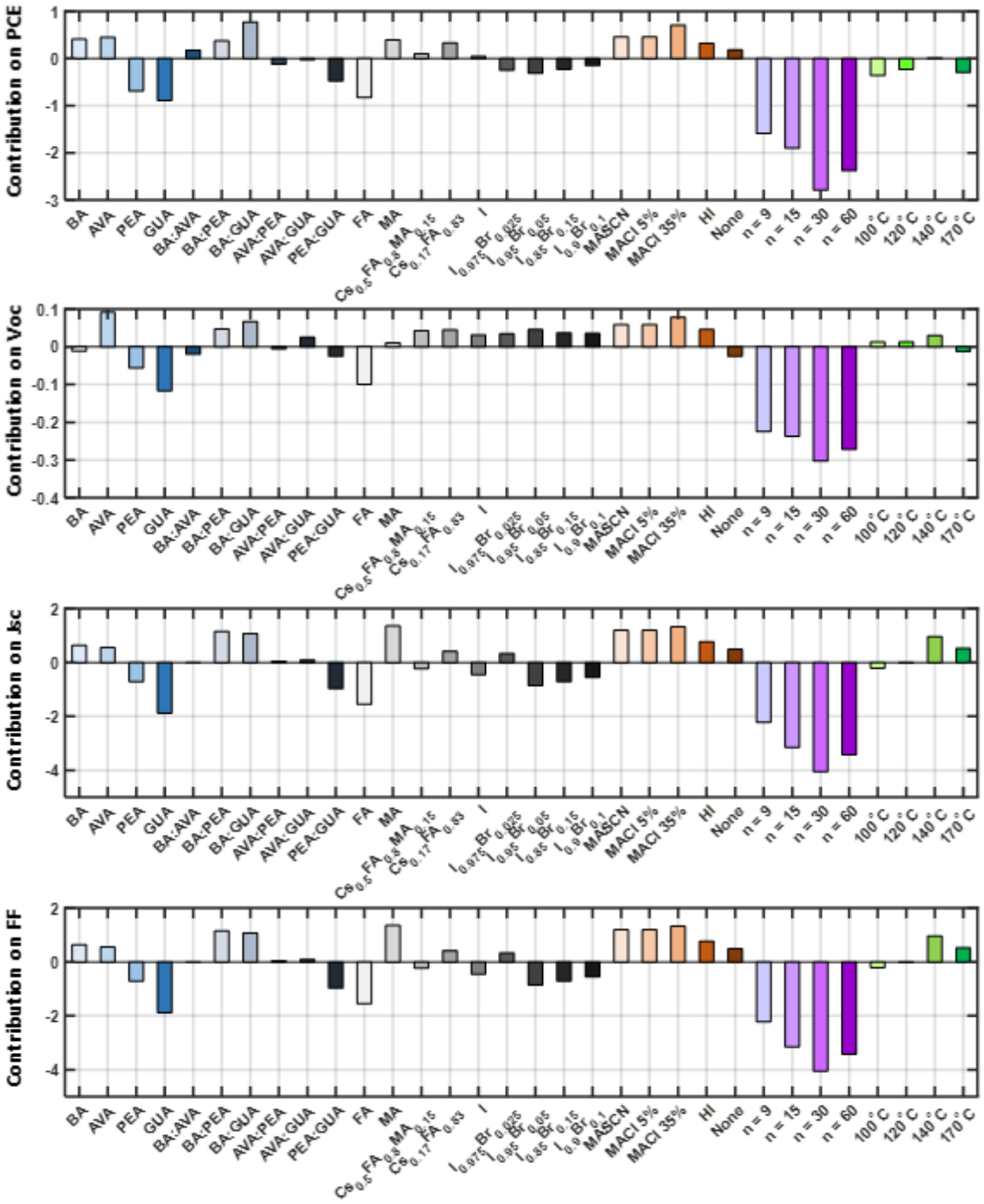

Figure 5. The effect and contribution of parameters on PCE, VOC, JSC and FF. Parameters with positive value increase the photovoltaics properties, and parameters with negative value decrease the PV properties.

The contribution effects indicated how certain modifications can in general increase or decrease PCE, V_{OC}, J_{SC}, and FF. For example, in the 2D cations category, the AVA can increase PCE, V_{OC}, J_{SC}, and FF, while PEA and GUA negatively impact all of them. The mixture of BA:PEA and BA:GUA positively impact all of them. The mixture of BA:AVA, AVA:PEA and AVA:GUA had very small impact on all properties. The mixture of PEA:GUA showed a negative effect on all properties. In summary, within the 2D cations category, GUA exhibited the largest negative effect while the mixture of BA:GUA showed the largest (or second largest) positive effect on PCE, V_{OC}, J_{SC}, and FF, as they have the largest negative and largest positive coefficients respectively.

In the 3D-cation category, FA showed the largest negative effect while MA indicated a very large positive impact on V_{OC} and FF and moderately positive effect on J_{SC} and PCE. The mixture of Cs0.17FA0.83 showed a consistent positive effect on PV properties.

In the halides category, the machine learning algorithm showed that adding bromine to iodine can decrease PCE while the opposite trend was shown for V_{OC}. Machine learning algorithms also demonstrate that including 0.025 bromine to iodine would increase J_{SC} and FF, while adding more bromine could decrease the aforementioned properties. Also, by comparing the coefficient contribution of iodine with hydrogen iodine, the PV properties will be increased. In summary, the 35%MACI has the largest positive effect on PCE, V_{OC} and J_{SC} while for FF the 5%MASCN has the largest positive contribution.

In terms of n number of options, there is a pattern that shows increasing the number of option from n=9 up to n=30 decreases the PV properties, while from n=30 to n=60 there is a less negative effect in PCE, V_{OC}, J_{SC} and FF. Machine learning algorithm also indicated that the temperature 140 °C is the optimum temperature for all PV properties.

2.4. Optimized recipe

In the final part of our study, we extracted and employed results from ML models to investigate the effect of fabrication parameters on PV properties. By only applying the parameters that can increase the property values shown in **Figure 6**, we obtained the champion recipe, which we used to fabricate the final batch of 2DRP PSCs. The final solar cells were tested for their performance (PCE, V_{OC}, J_{SC} and FF). The fabrication details can be found in the Experimental Section, and the performance metrics can be viewed in **Figure S10** in Supporting Information. A comparison between the photovoltaic properties of the new device based on the champion recipe suggested by machine learning (ML champion) with the experimental champion is shown in **Figure 7**.

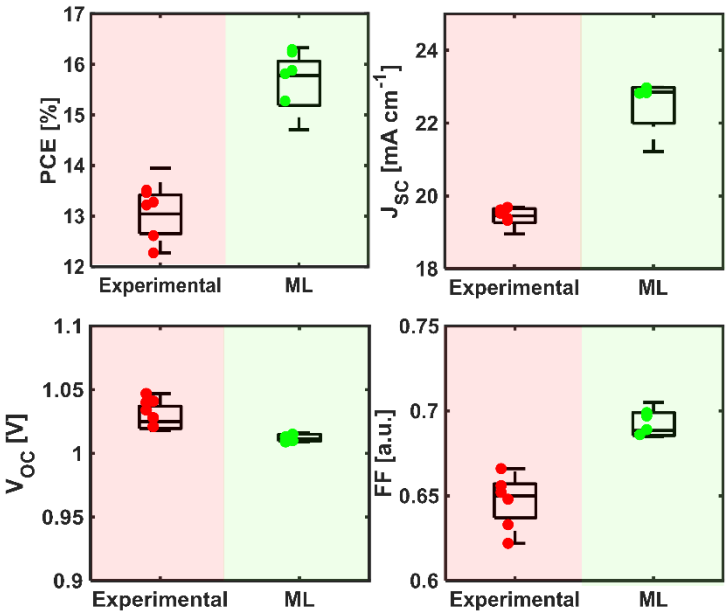

Figure 7. Comparison of the range of PV properties of the experimental champion with the ML champion.

For both experimental and ML champion, we measured the PV properties seven times and each time by forward and reverse measurement, and then compared the results. For PCE, J_{SC} and FF, the devices suggested by ML produced a higher PV values. Only for V_{OC} did the ML champion recipe exhibit a slightly lower value than the experimental champion. Notably, the

range of V_{OC} values for each measurement is minimal, which means that the V_{OC} values of this device are extremely reproducible.

3. Conclusions

Here we describe a new DoE with the combination of a bespoke ML protocol and a reproducible perovskite film fabrication technique that allows for rapid, combinatorial studies and screening of potentially hundreds of thousands of compositions. Our experimental cHTR system can be easily adopted and serve as an inexpensive, cross-reference tool for perovskite material fabrication. The automated approach reduces the sample-to-sample variation of manually produced materials, resulting in better precision of resulting films which could be directly fed into a ML protocol with high degree of trust. Notably, we have shown how the combination of automated perovskite film fabrication and ML modelling can rapidly generate unseen RPPs recipe with improved performance. The ML models elucidate the contributions of key fabrication parameters to make device performance characteristics, aiding the process of device improvement. The complete tracking of the key fabrication steps and conditions and automated performance measurements proposed here generated useful data to train ML models that were subsequently used to design improved PV materials. The insights from the ML models significantly shortened the discovery time and increased productivity. Importantly, our study revealed that some complex compositions, parameters, and additives can be synergistically screened which further accelerates progress in the perovskite photovoltaics. In comparison with manual fabrication, our methodology provides large improvements in the reproducibility and reliability of device manufacture. Moreover, our materials are made in similar conditions to manual drop-casting methods and hence can serve as a state-of-the-art comparison setup. The tracking of all parameters and precise precursor mixing allows for multiple tests and improvements, as well as staggered bleaching. ML protocols significantly

narrowed the distribution of parameters that had already been lowered by automation and facilitated fabrication of samples. These results pave the way for rapid, large-scale discovery studies where each fabrication step is carefully recorded and the complete protocol can be reproduced reliably without the variability inherent in manual methods. We have shown that such complex dissection of the fabrication process and automation of crucial steps allows for construction of data libraries that serve as cross-research group reference points and as training data for computational models. In summary, automated fabrication combined ML modeling allows the fabrication of optimal, efficient RPP films of high reproducibility that can be incorporated into devices with very good efficiencies and high long term environmental stability that can readily translate to industrialization of PSCs.

4. Experimental Section

General Information: Unless otherwise specified, all materials were purchased from Sigma-Aldrich.

Preparation of the Perovskite Precursor Solution: The perovskite precursor solution was prepared in a N_2-filled glovebox (MBraun, 0_2< 0.01ppm, H_2O<0.01 ppm) by mixing powders to a specified recipe in order to cover 100 different recipes described. As the stock solution anhydrous N,N-dimethylformamide (DMF), dimethyl sulfoxide (DMSO) and γ-Butyrolactone (GBL) were mixed in order to achieve 4:1:1 v/v. Stock solutions containing MASCN and MACl were produced by adding them proportionally in order to achieve specified concentrations in a 1 mL mixture (4:1:1 v/v) of anhydrous N,N-dimethylformamide (DMF), dimethyl sulfoxide (DMSO) and γ-Butyrolactone (GBL). The perovskite precursor solution and stock solutions were heated to 45 °C and magnetically stirred overnight until fully dissolved, subsequentially filtered with 0.45μm – directly prior the deposition all the solutions were passed through the microfluidic device described in Supporting Information.

Perovskite Solar Cell Fabrication: We used the same perovskite fabrication technique for both films and solar devices. Pre-cut and commercially pre-patterned ITO-coated soda lime glass substrates (Latech, 10 Ω cm^{-2}) were cleaned in sequence by sonication in: Milli-Q water (10 minutes at 25 °C), 2% Hellmanex® solution (10 minutes at 25 °C), acetone (10 minutes at 40 °C), isopropanol (15 minutes at 40 °C), ethanol (10 minutes at 25 °C). The substrates were subsequently treated with oxygen plasma for 12 minutes. We then fabricated ligand-modified NiO films employing method developed by Michalska and Surmiak *et al.*[57] Subsequentially, such prepared substrates with NiO films were transported to the glovebox with the system; they were then preheated on hot plate at 100 °C for 30 minutes and the N_2 was constantly applied onto the hot-plate area to remove residual H_2O. After that the substrates were brought to deposition pre-set temperature on programmable hot-plate stage. The precursor solution was pushed through the ultrasonic piezoelectric microfluidic device (see Supporting Information for more details) by programmable syringe pump (Chemyx 4000); the purity of the composition is ensured by emptying the dead volume from tubes (at least 3 times the tube length of 20 cm) into the purging waste container. Each pre-heated substrate located inside the cavity was blown with N_2 gas to remove any residual particles directly prior the deposition. Aliquots of 6 µL of perovskite precursor solution were deposited on the substrate and 10 seconds was allowed for the precursor solution to spread across the surface prior to quenching with an applied N_2 gas stream. The hot-plate was subsequently heated up to chosen annealing temperature, with the temperature maintained for 60 minutes, followed by cooling of the films naturally to RT. Samples to be used for complete device fabrication were transported in a sealed container into the evaporation glovebox. For complete devices, the perovskite edge was mechanically removed, followed by evaporation of fullerenes C_{60} (20 nm at 0.1 Å s^{-1} via thermal evaporation), C_{70} (10 nm at 0.1 Å s^{-1} via thermal evaporation), and then bathocuproine (3 nm

at 0.1 Å s^{-1} via thermal evaporation). The devices were completed by the evaporation of 65 nm of the gold electrode at 0.5 Å s^{-1} through the evaporation mask. The devices were stored in a N_2 glovebox for 1 day in the dark before characterization.

Performance characterization: The current density (*J-V*) characteristics of the devices were measured using a fully automated combinatorial high-throughput solar cell measurement system that was reported by us previously.[33] To simulate solar light, an ABET 3000 solar simulator with a xenon arc lamp, fed with 1000 W input power was used. The light intensity was calibrated using a professional reference silicon cell with an IR-cut off filter (KG5, Schott). The *J-V* curves were measured using a BioLogic VMP3 potentiostat in 4-wire sense configuration. All measurements (*J-V* dark, *J-V* light, stability and maximum power point tracking) were taken automatically without human interaction employing a high-throughput measurement technique developed by Surmiak et al.[33] A 5 minutes break was applied where the devices were cooled down by a laminar flow of N_2. The voltage step was set to 10 mV s^{-1}, starting voltage was in the reverse direction, and no bias conditioning or light soaking was applied. The working area of the devices was set to 0.1 cm^2.

Acknowledgements

The authors acknowledge the use of instruments and scientific and technical assistance at the Monash Centre for Electron Microscopy, a Node of Microscopy Australia. The authors acknowledge invaluable help and training of Dr Chuantian Zuo and Professor Mei Gao from CSIRO during the initial stage of this project. The authors acknowledge help provided by Dr Andrew Scully. The authors acknowledge the use of facilities and materials at CSIRO Flexible Electronics Laboratory. This work was performed in part at the Melbourne Centre for Nanofabrication (MCN) in the Victorian Node of the Australian National Fabrication Facility (ANFF). This work was performed in part at the South Australia node of the Australian National Fabrication Facility. A company established under the National Collaborative Research Infrastructure Strategy to provide nano and microfabrication facilities for Australia's researchers. The authors acknowledge use of the facilities and the assistance of Dr James Griffin at the Monash X-ray Platform.

References

1. NREL Best Research-Cell Efficiency Chart. (https://www.nrel.gov/pv/cell-efficiency.html.
2. Saliba, M.; Matsui, T.; Domanski, K.; Seo, J.-Y.; Ummadisingu, A.; Zakeeruddin, S. M.; Correa-Baena, J.-P.; Tress, W. R.; Abate, A.; Hagfeldt, A.; Grätzel, M., Incorporation of rubidium cations into perovskite solar cells improves photovoltaic performance. *Science* **2016,** *354* (6309), 206.
3. Travis, W.; Glover, E. N. K.; Bronstein, H.; Scanlon, D. O.; Palgrave, R. G., On the application of the tolerance factor to inorganic and hybrid halide perovskites: a revised system. *Chemical Science* **2016,** *7* (7), 4548-4556.
4. Jacobsson, T. J.; Pazoki, M.; Hagfeldt, A.; Edvinsson, T., Goldschmidt's Rules and Strontium Replacement in Lead Halogen Perovskite Solar Cells: Theory and Preliminary Experiments on CH3NH3SrI3. *The Journal of Physical Chemistry C* **2015,** *119* (46), 25673-25683.
5. Salado, M.; Contreras-Bernal, L.; Caliò, L.; Todinova, A.; López-Santos, C.; Ahmad, S.; Borras, A.; Idígoras, J.; Anta, J. A., Impact of moisture on efficiency-determining electronic processes in perovskite solar cells. *Journal of Materials Chemistry A* **2017,** *5* (22), 10917-10927.
6. Bryant, D.; Aristidou, N.; Pont, S.; Sanchez-Molina, I.; Chotchunangatchaval, T.; Wheeler, S.; Durrant, J. R.; Haque, S. A., Light and oxygen induced degradation limits the operational stability of methylammonium lead triiodide perovskite solar cells. *Energy & Environmental Science* **2016,** *9* (5), 1655-1660.
7. Ruan, S.; Surmiak, M.-A.; Ruan, Y.; McMeekin, D. P.; Ebendorff-Heidepriem, H.; Cheng, Y.-B.; Lu, J.; McNeill, C. R., Light induced degradation in mixed-halide perovskites. *Journal of Materials Chemistry C* **2019,** *7* (30), 9326-9334.
8. Misra, R. K.; Aharon, S.; Li, B.; Mogilyansky, D.; Visoly-Fisher, I.; Etgar, L.; Katz, E. A., Temperature- and Component-Dependent Degradation of Perovskite Photovoltaic Materials under Concentrated Sunlight. *The Journal of Physical Chemistry Letters* **2015,** *6* (3), 326-330.
9. Bae, S.; Kim, S.; Lee, S.-W.; Cho, K. J.; Park, S.; Lee, S.; Kang, Y.; Lee, H.-S.; Kim, D., Electric-Field-Induced Degradation of Methylammonium Lead Iodide Perovskite Solar Cells. *The Journal of Physical Chemistry Letters* **2016,** *7* (16), 3091-3096.
10. Chen, A. Z.; Shiu, M.; Deng, X.; Mahmoud, M.; Zhang, D.; Foley, B. J.; Lee, S.-H.; Giri, G.; Choi, J. J., Understanding the Formation of Vertical Orientation in Two-dimensional Metal Halide Perovskite Thin Films. *Chemistry of Materials* **2019,** *31* (4), 1336-1343.
11. Kahmann, S.; Tekelenburg, E. K.; Duim, H.; Kamminga, M. E.; Loi, M. A., Extrinsic nature of the broad photoluminescence in lead iodide-based Ruddlesden–Popper perovskites. *Nature Communications* **2020,** *11* (1), 2344.
12. Fu, Y.; Hautzinger, M. P.; Luo, Z.; Wang, F.; Pan, D.; Aristov, M. M.; Guzei, I. A.; Pan, A.; Zhu, X.; Jin, S., Incorporating Large A Cations into Lead Iodide Perovskite Cages: Relaxed Goldschmidt Tolerance Factor and Impact on Exciton–Phonon Interaction. *ACS Central Science* **2019,** *5* (8), 1377-1386.
13. Hartono, N. T. P.; Sun, S.; Gélvez-Rueda, M. C.; Pierone, P. J.; Erodici, M. P.; Yoo, J.; Wei, F.; Bawendi, M.; Grozema, F. C.; Sher, M.-j.; Buonassisi, T.; Correa-Baena, J.-P., The effect of structural dimensionality on carrier mobility in lead-halide perovskites. *Journal of Materials Chemistry A* **2019,** *7* (41), 23949-23957.

14. Stoumpos, C. C.; Cao, D. H.; Clark, D. J.; Young, J.; Rondinelli, J. M.; Jang, J. I.; Hupp, J. T.; Kanatzidis, M. G., Ruddlesden–Popper Hybrid Lead Iodide Perovskite 2D Homologous Semiconductors. *Chemistry of Materials* **2016,** *28* (8), 2852-2867.
15. Liu, Y.; Siron, M.; Lu, D.; Yang, J.; dos Reis, R.; Cui, F.; Gao, M.; Lai, M.; Lin, J.; Kong, Q.; Lei, T.; Kang, J.; Jin, J.; Ciston, J.; Yang, P., Self-Assembly of Two-Dimensional Perovskite Nanosheet Building Blocks into Ordered Ruddlesden–Popper Perovskite Phase. *Journal of the American Chemical Society* **2019,** *141* (33), 13028-13032.
16. Shi, J.; Gao, Y.; Gao, X.; Zhang, Y.; Zhang, J.; Jing, X.; Shao, M., Fluorinated Low-Dimensional Ruddlesden–Popper Perovskite Solar Cells with over 17% Power Conversion Efficiency and Improved Stability. *Advanced Materials* **2019,** *31* (37), 1901673.
17. Xu, Z.; Lu, D.; Liu, F.; Lai, H.; Wan, X.; Zhang, X.; Liu, Y.; Chen, Y., Phase Distribution and Carrier Dynamics in Multiple-Ring Aromatic Spacer-Based Two-Dimensional Ruddlesden–Popper Perovskite Solar Cells. *ACS Nano* **2020,** *14* (4), 4871-4881.
18. Chen, S.; Shen, N.; Zhang, L.; Zhang, L.; Cheung, S. H.; Chen, S.; So, S. K.; Xu, B., Understanding the Interplay of Binary Organic Spacer in Ruddlesden–Popper Perovskites toward Efficient and Stable Solar Cells. *Advanced Functional Materials* **2020,** *30* (10), 1907759.
19. Chen, H.; Xia, Y.; Wu, B.; Liu, F.; Niu, T.; Chao, L.; Xing, G.; Sum, T.; Chen, Y.; Huang, W., Critical role of chloride in organic ammonium spacer on the performance of Low-dimensional Ruddlesden-Popper perovskite solar cells. *Nano Energy* **2019,** *56*, 373-381.
20. Zheng, H.; Liu, D.; Wang, Y.; Yang, Y.; Li, H.; Zhang, T.; Chen, H.; Ji, L.; Chen, Z.; Li, S., Synergistic effect of additives on 2D perovskite film towards efficient and stable solar cell. *Chemical Engineering Journal* **2020,** *389*, 124266.
21. Gahlmann, T.; Brinkmann, K. O.; Becker, T.; Tückmantel, C.; Kreusel, C.; van gen Hassend, F.; Weber, S.; Riedl, T., Impermeable Charge Transport Layers Enable Aqueous Processing on Top of Perovskite Solar Cells. *Advanced Energy Materials* **2020,** *10* (10), 1903897.
22. Tavakoli, M. M.; Si, H.; Yadav, P.; Prochowicz, D.; Tavakoli, R., A Dopant-Free Hole Transporting Layer for Efficient and Stable Planar Perovskite Solar Cells. *physica status solidi (RRL) – Rapid Research Letters* **2020,** *14* (7), 2000147.
23. Svane, K. L.; Forse, A. C.; Grey, C. P.; Kieslich, G.; Cheetham, A. K.; Walsh, A.; Butler, K. T., How Strong Is the Hydrogen Bond in Hybrid Perovskites? *The Journal of Physical Chemistry Letters* **2017,** *8* (24), 6154-6159.
24. Du, Z. H.; Zhang, T. S.; Ma, J., Effect of polyvinylpyrrolidone on the formation of perovskite phase and rosette-like structure in sol-gel–derived PLZT films. *Journal of Materials Research* **2007,** *22* (8), 2195-2203.
25. Xiong, H.; DeLuca, G.; Rui, Y.; Zhang, B.; Li, Y.; Zhang, Q.; Wang, H.; Reichmanis, E., Modifying Perovskite Films with Polyvinylpyrrolidone for Ambient-Air-Stable Highly Bendable Solar Cells. *ACS Applied Materials & Interfaces* **2018,** *10* (41), 35385-35394.
26. Ramos-Terrón, S.; Jodlowski, A. D.; Verdugo-Escamilla, C.; Camacho, L.; de Miguel, G., Relaxing the Goldschmidt Tolerance Factor: Sizable Incorporation of the Guanidinium Cation into a Two-Dimensional Ruddlesden–Popper Perovskite. *Chemistry of Materials* **2020,** *32* (9), 4024-4037.
27. Pan, H.; Zhao, X.; Gong, X.; Shen, Y.; Wang, M., Atomic-Scale Tailoring of Organic Cation of Layered Ruddlesden–Popper Perovskite Compounds. *The Journal of Physical Chemistry Letters* **2019,** *10* (8), 1813-1819.
28. Qing, J.; Kuang, C.; Wang, H.; Wang, Y.; Liu, X.-K.; Bai, S.; Li, M.; Sum, T. C.; Hu, Z.; Zhang, W.; Gao, F., High-Quality Ruddlesden–Popper Perovskite Films Based on In Situ Formed Organic Spacer Cations. *Advanced Materials* **2019,** *31* (41), 1904243.

29. Li, Y.; Cheng, H.; Zhao, K.; Wang, Z.-S., 4-(Aminoethyl)pyridine as a Bifunctional Spacer Cation for Efficient and Stable 2D Ruddlesden–Popper Perovskite Solar Cells. *ACS Applied Materials & Interfaces* **2019,** *11* (41), 37804-37811.
30. Mao, P.; Zhuang, J.; Wei, Y.; Chen, N.; Luan, Y.; Wang, J., Origin and Suppression of the Graded Phase Distribution in Ruddlesden-Popper Perovskite Films for Photovoltaic Application. *Solar RRL* **2019,** *3* (4), 1800357.
31. Dong, Y.; Lu, D.; Xu, Z.; Lai, H.; Liu, Y., 2-Thiopheneformamidinium-Based 2D Ruddlesden–Popper Perovskite Solar Cells with Efficiency of 16.72% and Negligible Hysteresis. *Advanced Energy Materials* **2020,** *10* (28), 2000694.
32. Liang, C.; Zhao, D.; Li, Y.; Li, X.; Peng, S.; Shao, G.; Xing, G., Ruddlesden–Popper Perovskite for Stable Solar Cells. *ENERGY & ENVIRONMENTAL MATERIALS* **2018,** *1* (4), 221-231.
33. Surmiak, M. A.; Zhang, T.; Lu, J.; Rietwyk, K. J.; Raga, S. R.; McMeekin, D. P.; Bach, U., High-Throughput Characterization of Perovskite Solar Cells for Rapid Combinatorial Screening. *Solar RRL* **2020,** *4* (7), 2000097.
34. Park, N.-G.; Zhu, K., Scalable fabrication and coating methods for perovskite solar cells and solar modules. *Nature Reviews Materials* **2020,** *5* (5), 333-350.
35. Li, Z.; Klein, T. R.; Kim, D. H.; Yang, M.; Berry, J. J.; van Hest, M. F. A. M.; Zhu, K., Scalable fabrication of perovskite solar cells. *Nature Reviews Materials* **2018,** *3* (4), 18017.
36. Kim, J. H.; Williams, S. T.; Cho, N.; Chueh, C.-C.; Jen, A. K. Y., Enhanced Environmental Stability of Planar Heterojunction Perovskite Solar Cells Based on Blade-Coating. *Advanced Energy Materials* **2015,** *5* (4), 1401229.
37. Razza, S.; Di Giacomo, F.; Matteocci, F.; Cinà, L.; Palma, A. L.; Casaluci, S.; Cameron, P.; D'Epifanio, A.; Licoccia, S.; Reale, A.; Brown, T. M.; Di Carlo, A., Perovskite solar cells and large area modules (100 cm2) based on an air flow-assisted PbI2 blade coating deposition process. *Journal of Power Sources* **2015,** *277*, 286-291.
38. Bishop, J. E.; Routledge, T. J.; Lidzey, D. G., Advances in Spray-Cast Perovskite Solar Cells. *The Journal of Physical Chemistry Letters* **2018,** *9* (8), 1977-1984.
39. Bishop, J. E.; Read, C. D.; Smith, J. A.; Routledge, T. J.; Lidzey, D. G., Fully Spray-Coated Triple-Cation Perovskite Solar Cells. *Scientific Reports* **2020,** *10* (1), 6610.
40. Mathies, F.; Eggers, H.; Richards, B. S.; Hernandez-Sosa, G.; Lemmer, U.; Paetzold, U. W., Inkjet-Printed Triple Cation Perovskite Solar Cells. *ACS Applied Energy Materials* **2018,** *1* (5), 1834-1839.
41. Eggers, H.; Schackmar, F.; Abzieher, T.; Sun, Q.; Lemmer, U.; Vaynzof, Y.; Richards, B. S.; Hernandez-Sosa, G.; Paetzold, U. W., Inkjet-Printed Micrometer-Thick Perovskite Solar Cells with Large Columnar Grains. *Advanced Energy Materials* **2020,** *10* (6), 1903184.
42. Hwang, K.; Jung, Y.-S.; Heo, Y.-J.; Scholes, F. H.; Watkins, S. E.; Subbiah, J.; Jones, D. J.; Kim, D.-Y.; Vak, D., Toward Large Scale Roll-to-Roll Production of Fully Printed Perovskite Solar Cells. *Advanced Materials* **2015,** *27* (7), 1241-1247.
43. Dou, B.; Whitaker, J. B.; Bruening, K.; Moore, D. T.; Wheeler, L. M.; Ryter, J.; Breslin, N. J.; Berry, J. J.; Garner, S. M.; Barnes, F. S.; Shaheen, S. E.; Tassone, C. J.; Zhu, K.; van Hest, M. F. A. M., Roll-to-Roll Printing of Perovskite Solar Cells. *ACS Energy Letters* **2018,** *3* (10), 2558-2565.
44. Chen, C.-W.; Kang, H.-W.; Hsiao, S.-Y.; Yang, P.-F.; Chiang, K.-M.; Lin, H.-W., Efficient and Uniform Planar-Type Perovskite Solar Cells by Simple Sequential Vacuum Deposition. *Advanced Materials* **2014,** *26* (38), 6647-6652.
45. Hsiao, S.-Y.; Lin, H.-L.; Lee, W.-H.; Tsai, W.-L.; Chiang, K.-M.; Liao, W.-Y.; Ren-Wu, C.-Z.; Chen, C.-Y.; Lin, H.-W., Efficient All-Vacuum Deposited Perovskite Solar Cells

by Controlling Reagent Partial Pressure in High Vacuum. *Advanced Materials* **2016,** *28* (32), 7013-7019.
46. Zhou, N.; Shen, Y.; Li, L.; Tan, S.; Liu, N.; Zheng, G.; Chen, Q.; Zhou, H., Exploration of Crystallization Kinetics in Quasi Two-Dimensional Perovskite and High Performance Solar Cells. *Journal of the American Chemical Society* **2018,** *140* (1), 459-465.
47. Mathies, F.; List-Kratochvil, E. J. W.; Unger, E. L., Advances in Inkjet-Printed Metal Halide Perovskite Photovoltaic and Optoelectronic Devices. *Energy Technology* **2020,** *8* (4), 1900991.
48. Chen, Y.; Li, N.; Wang, L.; Li, L.; Xu, Z.; Jiao, H.; Liu, P.; Zhu, C.; Zai, H.; Sun, M.; Zou, W.; Zhang, S.; Xing, G.; Liu, X.; Wang, J.; Li, D.; Huang, B.; Chen, Q.; Zhou, H., Impacts of alkaline on the defects property and crystallization kinetics in perovskite solar cells. *Nature Communications* **2019,** *10* (1), 1112.
49. Chen, S.; Zhang, L.; Yan, L.; Xiang, X.; Zhao, X.; Yang, S.; Xu, B., Accelerating the Screening of Perovskite Compositions for Photovoltaic Applications through High-Throughput Inkjet Printing. *Advanced Functional Materials* **2019,** *29* (49), 1905487.
50. Jacobsson, T. J.; Hultqvist, A.; García-Fernández, A.; Anand, A.; Al-Ashouri, A.; Hagfeldt, A.; Crovetto, A.; Abate, A.; Ricciardulli, A. G.; Vijayan, A.; Kulkarni, A.; Anderson, A. Y.; Darwich, B. P.; Yang, B.; Coles, B. L.; Perini, C. A. R.; Rehermann, C.; Ramirez, D.; Fairen-Jimenez, D.; Di Girolamo, D.; Jia, D.; Avila, E.; Juarez-Perez, E. J.; Baumann, F.; Mathies, F.; González, G. S. A.; Boschloo, G.; Nasti, G.; Paramasivam, G.; Martínez-Denegri, G.; Näsström, H.; Michaels, H.; Köbler, H.; Wu, H.; Benesperi, I.; Dar, M. I.; Bayrak Pehlivan, I.; Gould, I. E.; Vagott, J. N.; Dagar, J.; Kettle, J.; Yang, J.; Li, J.; Smith, J. A.; Pascual, J.; Jerónimo-Rendón, J. J.; Montoya, J. F.; Correa-Baena, J.-P.; Qiu, J.; Wang, J.; Sveinbjörnsson, K.; Hirselandt, K.; Dey, K.; Frohna, K.; Mathies, L.; Castriotta, L. A.; Aldamasy, M. H.; Vasquez-Montoya, M.; Ruiz-Preciado, M. A.; Flatken, M. A.; Khenkin, M. V.; Grischek, M.; Kedia, M.; Saliba, M.; Anaya, M.; Veldhoen, M.; Arora, N.; Shargaieva, O.; Maus, O.; Game, O. S.; Yudilevich, O.; Fassl, P.; Zhou, Q.; Betancur, R.; Munir, R.; Patidar, R.; Stranks, S. D.; Alam, S.; Kar, S.; Unold, T.; Abzieher, T.; Edvinsson, T.; David, T. W.; Paetzold, U. W.; Zia, W.; Fu, W.; Zuo, W.; Schröder, V. R. F.; Tress, W.; Zhang, X.; Chiang, Y.-H.; Iqbal, Z.; Xie, Z.; Unger, E., An open-access database and analysis tool for perovskite solar cells based on the FAIR data principles. *Nature Energy* **2022,** *7* (1), 107-115.
51. Lee, J.; Lee, W.; Lee, J.; Baek, K.-Y.; Shin, J.; Kim, J.-K.; Kim, J.; Ahn, H.; Kang, K.; Lee, T., Tailored Design-of-Experiments Approach for Device Performance Prediction and Optimization of Flash-Evaporated Organic–Inorganic Halide Perovskite-Based Photodetectors. *Advanced Materials Technologies* **2021,** *6* (5), 2001131.
52. Zuo, C.; Scully, A. D.; Tan, W. L.; Zheng, F.; Ghiggino, K. P.; Vak, D.; Weerasinghe, H.; McNeill, C. R.; Angmo, D.; Chesman, A. S. R.; Gao, M., Crystallisation control of drop-cast quasi-2D/3D perovskite layers for efficient solar cells. *Communications Materials* **2020,** *1* (1), 33.
53. Zuo, C.; Vak, D.; Angmo, D.; Ding, L.; Gao, M., One-step roll-to-roll air processed high efficiency perovskite solar cells. *Nano Energy* **2018,** *46*, 185-192.
54. Zuo, C.; Scully, A. D.; Gao, M., Drop-Casting Method to Screen Ruddlesden–Popper Perovskite Formulations for Use in Solar Cells. *ACS Applied Materials & Interfaces* **2021,** *13* (47), 56217-56225.
55. Fang, H.-H.; Adjokatse, S.; Wei, H.; Yang, J.; Blake, G. R.; Huang, J.; Even, J.; Loi, M. A., Ultrahigh sensitivity of methylammonium lead tribromide perovskite single crystals to environmental gases. *Science Advances* **2016,** *2* (7), e1600534.
56. Liu, X.; He, J.; Wang, P.; Liu, Y.; Xiao, J.; Ku, Z.; Peng, Y.; Huang, F.; Cheng, Y.-B.; Zhong, J., Fabrication of Efficient and Stable Perovskite Solar Cells in High-Humidity

Environment through Trace-Doping of Large-Sized Cations. *ChemSusChem* **2019,** *12* (11), 2385-2392.
57. Michalska, M.; Surmiak, M. A.; Maasoumi, F.; Senevirathna, D. C.; Chantler, P.; Li, H.; Li, B.; Zhang, T.; Lin, X.; Deng, H.; Chandrasekaran, N.; Peiris, T. A. N.; Rietwyk, K. J.; Chesman, A. S. R.; Alan, T.; Vak, D.; Bach, U.; Jasieniak, J. J., Microfluidic Processing of Ligand-Engineered NiO Nanoparticles for Low-Temperature Hole-Transporting Layers in Perovskite Solar Cells. *Solar RRL* **2021,** *5* (8), 2100342.
58. Meftahi, N.; Klymenko, M.; Christofferson, A. J.; Bach, U.; Winkler, D. A.; Russo, S. P., Machine learning property prediction for organic photovoltaic devices. *npj Computational Materials* **2020,** *6* (1), 166.
59. Tao, Q.; Xu, P.; Li, M.; Lu, W., Machine learning for perovskite materials design and discovery. *npj Computational Materials* **2021,** *7* (1), 23.
60. Howard, J. M.; Tennyson, E. M.; Neves, B. R. A.; Leite, M. S., Machine Learning for Perovskites' Reap-Rest-Recovery Cycle. *Joule* **2019,** *3* (2), 325-337.
61. SURMIAK, M. A. High-Throughput Perovskite Solar Cell Materials Discovery. Monash University, 2021.
62. Sun, J.; Lu, J.; Li, B.; Jiang, L.; Chesman, A. S. R.; Scully, A. D.; Gengenbach, T. R.; Cheng, Y.-B.; Jasieniak, J. J., Inverted perovskite solar cells with high fill-factors featuring chemical bath deposited mesoporous NiO hole transporting layers. *Nano Energy* **2018,** *49*, 163-171.
63. Figueiredo, M. r. A. T., Adaptive Sparseness for Supervised Learning. *IEEE Trans. Pattern Anal. Mach. Intell.* **2003,** *25*, 1150-1159.
64. Burden, F. R.; Winkler, D. A., New QSAR Methods Applied to Structure−Activity Mapping and Combinatorial Chemistry. *Journal of Chemical Information and Computer Sciences* **1999,** *39* (2), 236-242.
65. Burden, F. R.; Winkler, D. A., Robust QSAR Models Using Bayesian Regularized Neural Networks. *Journal of Medicinal Chemistry* **1999,** *42* (16), 3183-3187.
66. Winkler, D. A.; Burden, F. R., Robust QSAR Models from Novel Descriptors and Bayesian Regularised Neural Networks. *Molecular Simulation* **2000,** *24* (4-6), 243-258.
67. Gauraha, N., Introduction to the LASSO. *Resonance* **2018,** *23* (4), 439-464.
68. Tibshirani, R., Regression Shrinkage and Selection Via the Lasso. *Journal of the Royal Statistical Society: Series B (Methodological)* **1996,** *58* (1), 267-288.
69. Katritzky, A. R.; Kuanar, M.; Slavov, S.; Hall, C. D.; Karelson, M.; Kahn, I.; Dobchev, D. A., Quantitative Correlation of Physical and Chemical Properties with Chemical Structure: Utility for Prediction. *Chemical Reviews* **2010,** *110* (10), 5714-5789.
70. Wold, S.; Eriksson, L.; Clementi, S., Statistical Validation of QSAR Results. In *Chemometric Methods in Molecular Design*, 1995; pp 309-338.

Supporting Information

Machine Learning-Enhanced High-Throughput Fabrication and Optimization of Quasi-2D Ruddlesden-Popper Perovskite Solar Cells

Nastaran Meftahi,,† Maciej Adam Surmiak,*,† Sebastian O. Fürer, Kevin James Rietwyk, Jianfeng Lu, Sonia Ruiz Raga, Caria Evans, Monika Michalska, Hao Deng, David P. McMeekin, Tuncay Alan, Dechan Angmo, Doojin Vak, Anthony Chesman, Andrew J. Christofferson, David A. Winkler, Udo Bach, and Salvy P. Russo*

Dr. N. Meftahi, Dr. A. J. Christofferson and Prof. Salvy Russo
ARC Centre of Excellence in Exciton Science, School of Science, RMIT University, Melbourne, Victoria 3001, Australia
E-mail: nastaran.meftahi@rmit.edu.au

Dr. M. A. Surmiak, Dr. S. O. Furer, Dr. K. J. Rietwyk, Dr S. R. Raga, Dr. J. Lu, Ms. M. Michalska, Dr. D. P. McMeekin and Prof. U. Bach
Department of Chemical and Biological Engineering, Monash University, Victoria 3800, Australia
ARC Centre of Excellence for Exciton Science, Monash University, Victoria 3800, Australia
E-mail: adam.surmiak@monash.edu

Dr. D. Angmo, Dr. D. Vak, Dr. A. Chesman and Dr. M. A. Surmiak
CSIRO Manufacturing, Clayton, Victoria 3168, Australia

Dr. J. Lu
State Key Laboratory of Advanced Technology for Materials Synthesis and Processing, Wuhan University of Technology, Wuhan 430070, China

H. Deng, Dr T. Alan
Department of Mechanical and Aerospace Engineering, Faculty of Engineering, Monash University, Clayton, Victoria 3800, Australia

H. Deng
Department of Material Science and Engineering, Monash University, Clayton, Victoria 3800, Australia

Caria Evans
School of Chemistry and Biochemistry, Georgia Institute of Technology, Atlanta, Georgia 30332, United States

Prof. David A. Winkler
Department of Biochemistry and Chemistry, La Trobe Institute for Molecular Science, La Trobe University, Melbourne, Victoria 3086, Australia
School of Pharmacy, University of Nottingham, Nottingham NG7 2RD, United Kingdom

*Corresponding authors
†These authors contributed equally

SECTION 1. More on RPP perovskites and deposition technique development

Three-dimensional (3D) perovskite solar cells (PSC) reached power conversion efficiencies (PCE) of up to 25.5% in 2020, an impressive achievement given their relatively short development period. Despite their advantages over state-of-art silicon solar cells (26.2%), such as low fabrication costs, reduced energy requirements during the manufacturing process, and band-gap tunability, there remain significant challenges, namely, long-term operational stability, poor reproducibility and anomalous hysteretic behavior. Poor device stability is one of the main limiting factors preventing this class of solar cell from being commercialized. While thermal and moisture degradation can be minimized using encapsulation, additives or moisture- and oxygen-free fabrication environments, further degradation mechanisms have been reported. These include halide segregation, UV-light induced degradation, ionic movements, decomposition of complex inorganic-organic structures and problems induced by electrical stress. For commercialization of PSCs to be realized, research focus should not be limited to maximizing the efficiency on a smaller laboratory scale, but should be expanded to routinely include inexpensive materials that are deposited with industry-compatible production methods. Typically, most electron and hole accepting layers, along with the perovskite layer itself, are deposited by spin coating, which is not suitable for large-scale or high-throughput applications. To overcome this hurdle, a number of deposition techniques have been employed for PSC fabrication, such as blade coating, spray deposition, roll-to-roll printing, ink-jet printing and vacuum deposition techniques. While these methods provide a pathway towards commercialization, several challenges still remain. In particular, small variations in wettability, thickness, roughness and morphology causes non-uniformities over large areas, with these variations causing shunts, or even pinholes, which can short-circuit the device. There exist many trade-offs between each deposition techniques; for instance, large-area vacuum deposition techniques allow for accurate thickness control while limiting the number of voids, however, they suffer from low deposition rates and require high-vacuum, causing often uncontrollable phase transformations. There are multiple vacuum-free PSC fabrication techniques such as printing (ink-jet, roll-to-roll, doctor blading), gas pump method, gas-knife blading or dip-coating, all are suitable alternatives to high-vacuum deposition. An interesting method was employed in 2019 by Zuo *et al*., who used a simple drop casting methodology on mildly preheated substrates for perovskite fabrication. The authors demonstrated that by simply lowering the concentration of the perovskite precursor solution (< 0.5 M), the solution could spread more evenly across the substrate and form self-assembled, vertically oriented and

efficient perovskite films. Remarkably, such a simple technique creates new opportunities for rapid compositional screening using drop-cast precursor solutions to form high quality perovskite films. The reproducibility of PSC fabrication is severely hindered by subtle changes in environmental conditions during deposition, which is likely to impact negatively on the optimization of the fabrication process. Avoiding this can be accomplished by partial or complete removal of manual handling and human error. Drop casting is a simple deposition technique that is compatible with a combinatorial high-throughput research (cHTR) approach, where key parameters can be controlled, allowing for highly reproducible results. cHTR systems have been applied to PSC research in order to screen the large parameter space created by the compositional variety of perovskite materials. Importantly, cHTR systems have been used to synthesize and characterize new perovskite materials. Current cHTR methods for perovskite fabrication include: miniature crystallization cuvettes, ink-jet sprays, solvent screening pipettes or spray-pyrolysis nozzles. Such systems allow researchers to accelerate the discovery process of perovskite compositions and their optimum fabrication conditions. The importance of predicting and screening new perovskite materials whilst recording the data into a concise materials library is essential. Manual fabrication attempts for large parameter space screenings related to wide band gap exploration and tandem silicon-perovskite devices were demonstrated in 2017 by Jacobsson *et al*. Continuing on this path, Chen *et al*. used a robotic system to create a compositional map for the $FA_{1-x}Cs_xPb(I_{1-x}Br_x)_3$ perovskite system in order to find the optimum composition for a wide-band gap material for tandem solar cells applications. Wide band gap perovskite materials are of particular interest as a front-cell in a tandem silicon-perovskite solar cell (TSPSC), which have demonstrated significant commercial potential by reaching > 29.1 % PCE in 2020. In particular, two dimensional (2D) perovskites have emerged as a critical component for TSPSC applications due to their excellent stabilities. Similarly to their 3D counterparts, the band gap of 2D perovskites can be tuned by halide substitution. The interesting properties of 2D materials led Tsai *et al*. to propose a hot casting method for fabricating 2D Ruddlesden-Popper (R-P) perovskites crystal structures, allowing for an increase in the PCE from <5 % to a more promising 12.52 %. Further studies by Stoumpos *et al*. provided a library of crystallographic and photophysical properties of 2D R-P perovskites through a systematic change in the precursor stoichiometry, the synthesis and characterization of R-P crystals ranging from stochiometric index (n): n = 1, 2, 3, 4 and ∞. For example, a photoluminescence and UV-vis absorption spectra study revealed that the R-P perovskite band gap can be tuned by changing the chemical composition with formula $R_2A_{n-1}M_nX_{3n+1}$, where R is a bulky organic cation, A an alkali metal or organic cation, M a group

IVA metal and X a halogen (e.g. iodide or bromide). The R-P perovskite precursor solution crystallizes into a layered structure where 3D "packed" <100> crystal units are separated by 2D layers, where ammonium spacer cations replace an A-site cation. It is worthwhile noting that in 2020 Ren *et al*. revealed the intra-layer molecular interactions of 2D R-P, further ushering those perovskites to the group of next emerging candidates for photostable, defect-free and low hysteric candidates. Their work provided an interesting insight into fabrication methodology of highly performing 2D R-P perovskites, which are now reaching a competitive PCE of >18 %. We present in **Figures S1 and S2**, illustrations of the crystal structure for various n-numbers and its conceptual orientation to the substrate.

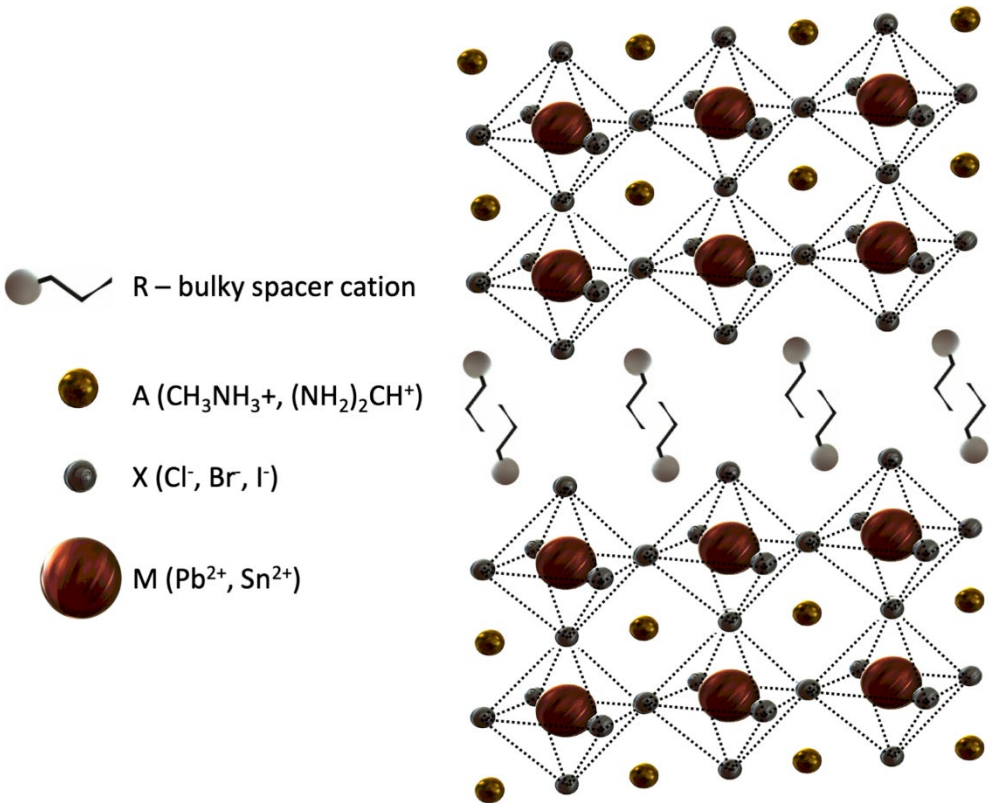

Figure S1. Crystal structure of quasi-2D Ruddlesden-Popper perovskite where R^+ (bulky cation spacer) intercalates in the crystal lattice resulting in the enhancement of the structure stability.

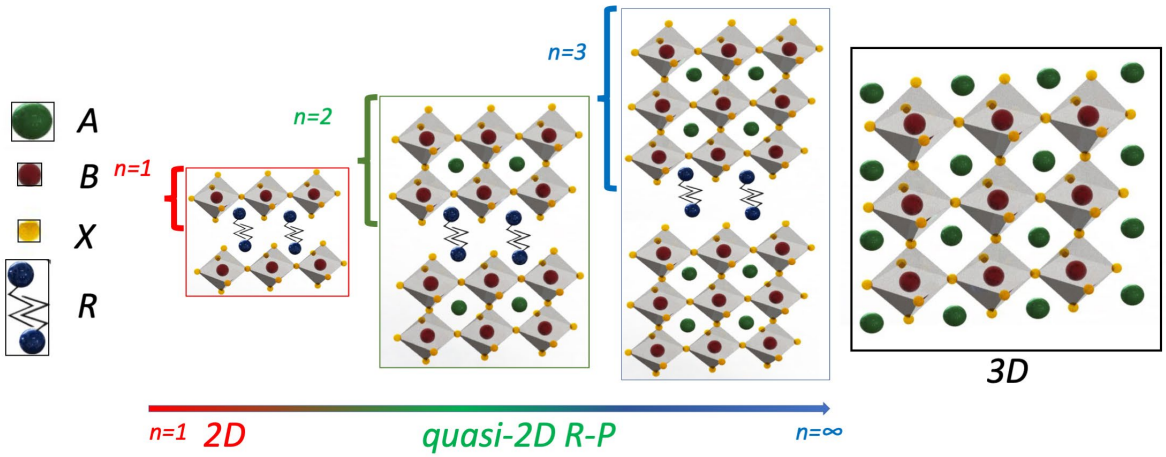

Figure S2. Schematic of the crystal structure evolution of 2D to 3D perovskites. A layered perovskite crystal structure for n-number = 1, 2, 3. The pure 2D-perovskite has the chemical formula R_2BX_4, the quasi-2D Ruddlesden-Popper structure $R_2A_{n-1}M_nX_{3n+1}$. The n-number of the quasi-2D R-P PSC perovskites indicates the number of 3D perovskite layers separated by the bulky cation spacer layers, with n = ∞ giving a conventional 3D perovskite.

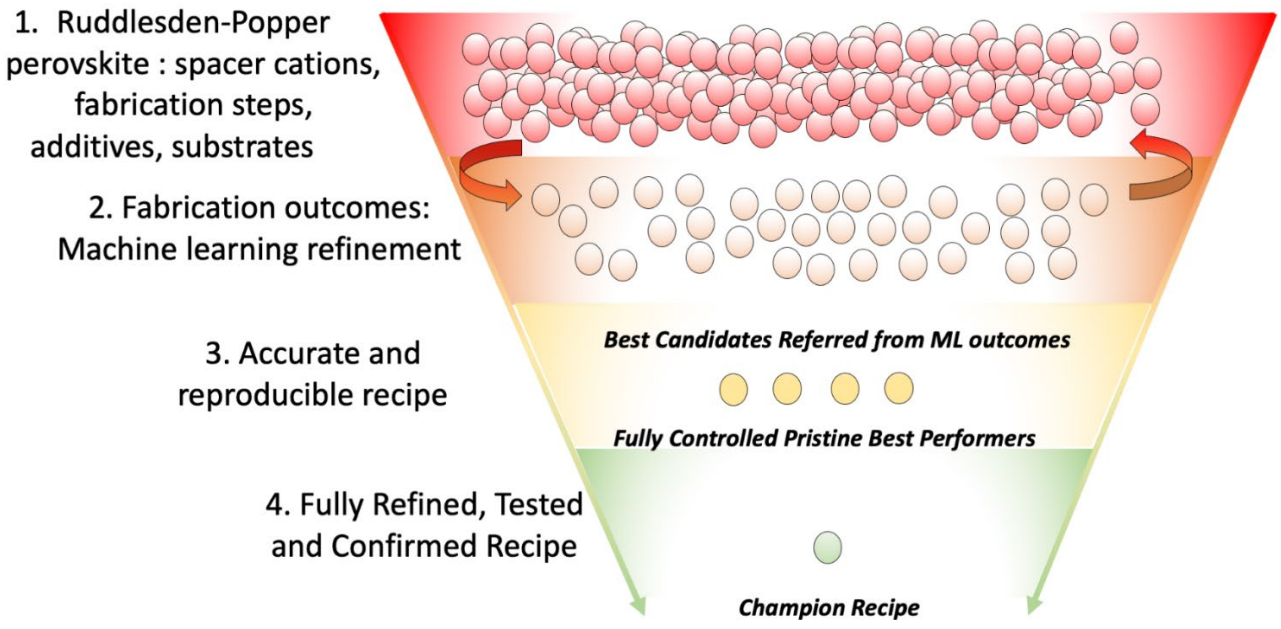

Figure S3. Illustration of the process workflow with machine learning enhancement for narrowing down and accelerating the RPP recipe optimization. Each circle represents a batch of experiments.

Section 2. PEROVSKITE PREPARATION

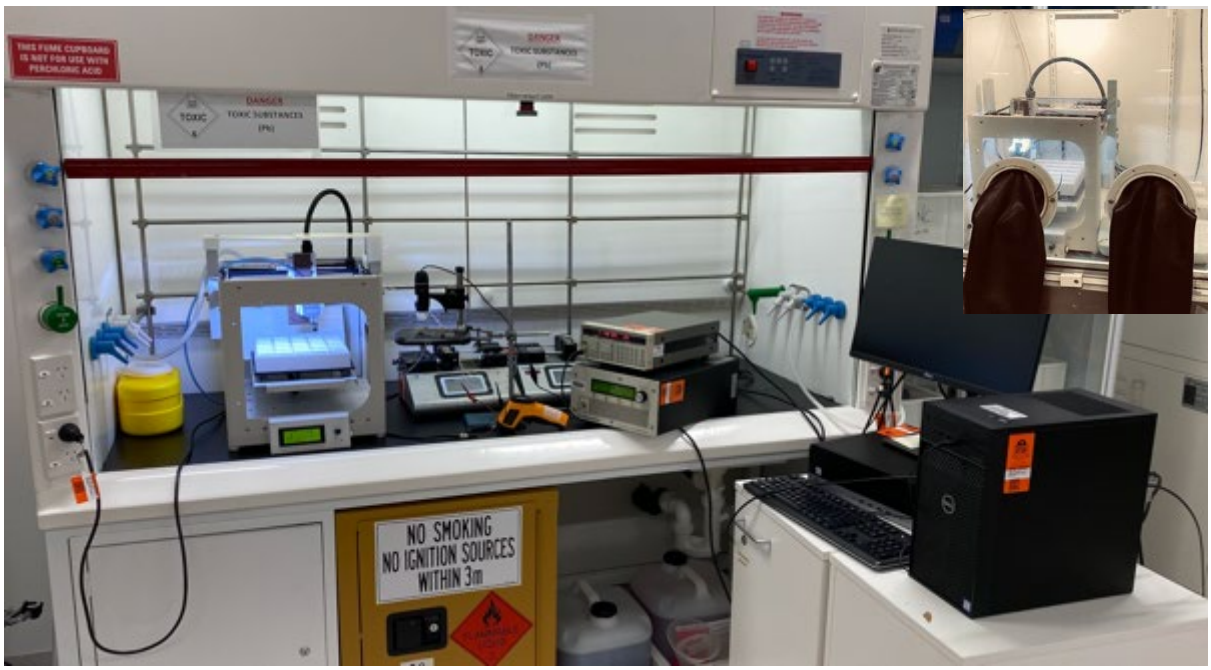

Figure S4. Combinatorial High-Throughput system overview (testing stage before building it into glovebox). System consists of: XYZ stage with programmable hotplate, deposition head with needle, dual syringe programmable pumps, PC with algorithms for control.

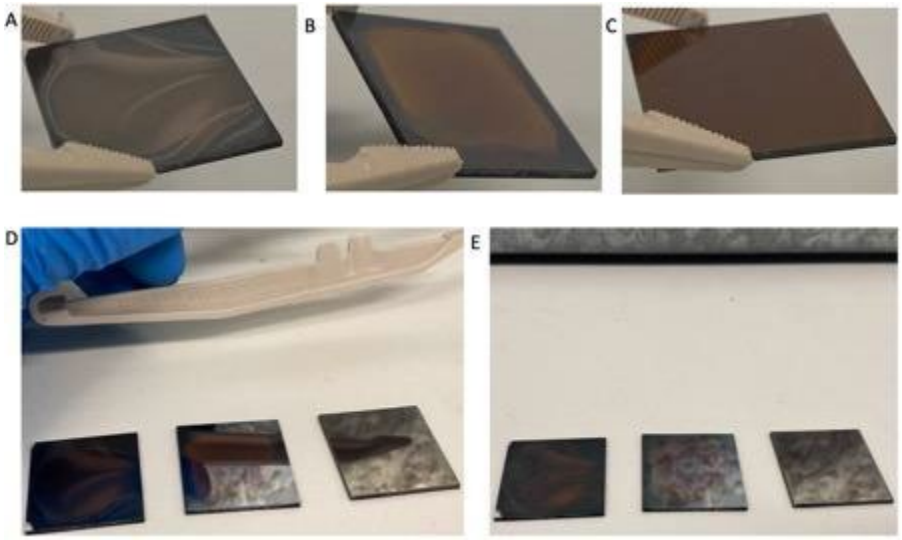

Figure S5. Films fabricated by the automated system inside of the 3D printed cavities. A) Nonuniform, "self-assembled" film without gas quenching. B) Uniform film with a "coffee ring" edge effect. C) Optimized through solvent engineering precursor solution resulting in significant or complete reduction of the "coffee ring" edge effect. D,E) Lack of timely employed gas quenching results in rough film, whereas the gas quenched films exhibit "mirror" like finish.

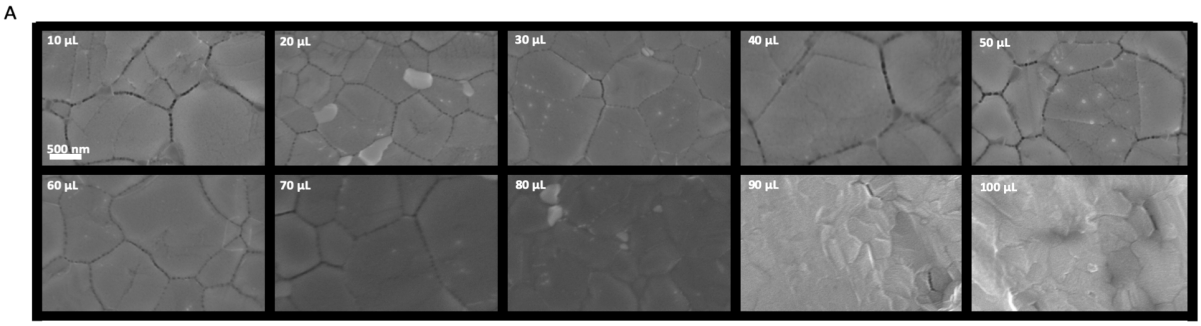

Figure S6. SEM micrograms illustrating surface morphology of the films obtained by solvent exchange: DMF replaced with GBL (exchanged volume in top left corner of each microgram).

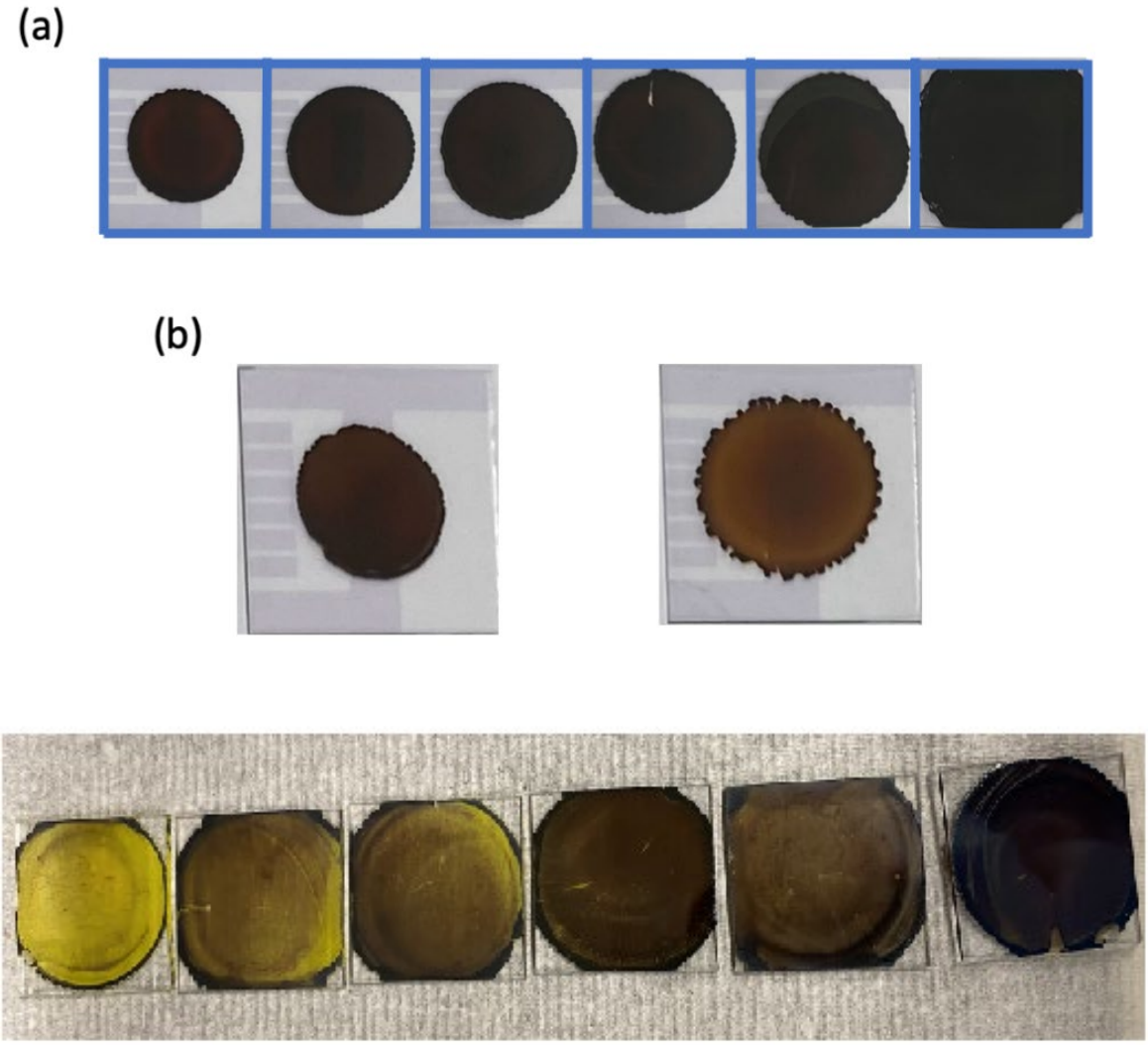

Figure S7. Sample cell images.

The authors in this particular work employed this novel device only to directly homogenize and agitate 1 solution type at a time (connecting two syringes pre-filled with the same solution).

The piezoelectric actuated active acoutofluidic device. The device homogenies precursors within milliseconds, ultimately allowing for ad-hoc high pressure, high agitation, and low volume mixing. The operating principle of the device is to actuate the silicon-oscillator at 1.06 MHz through the piezoelectric transducer (PZ26, Ferroperm Piezo-ceramics, Meggitt) using the function generator (Stanford Research Systems DS345) and amplifier (T&C Power Conversion, Inc. 229 AG 1006). During operation, a 1.06 MHz 1.37 W sinusoidal electric signal causes the membrane structure to resonate and thus rapidly homogenizes solutions. The device was flushed with a 20 mL of stock solution: (4:1:1 v/v) of anhydrous N,N-dimethylformamide (DMF), dimethyl sulfoxide (DMSO) and γ-Butyrolactone (GBL). More details and exact device fabrication specification can be found here.[1]

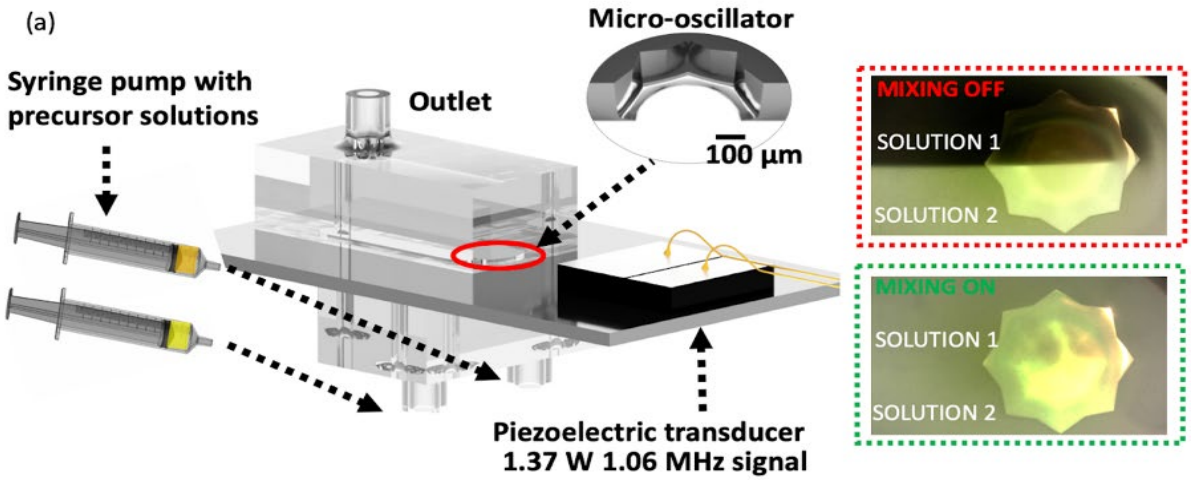

Figure S8. Device schematic.

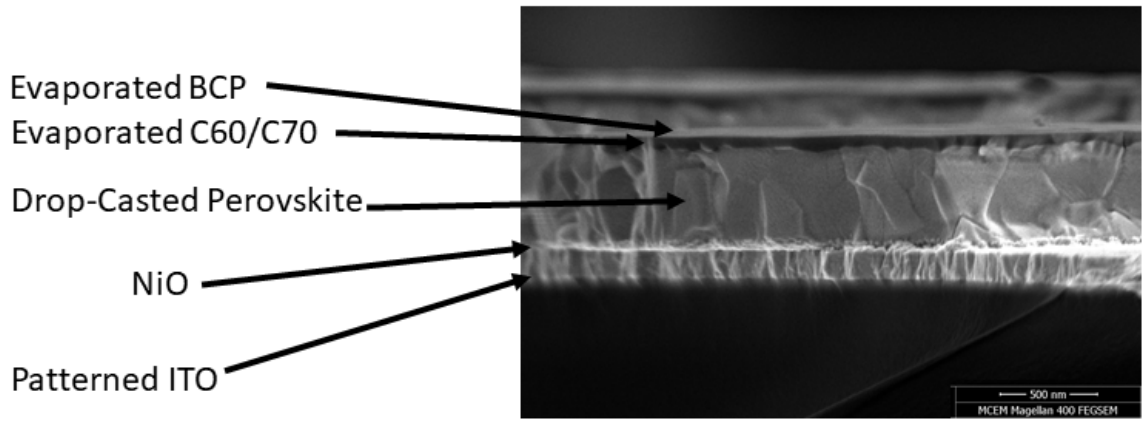

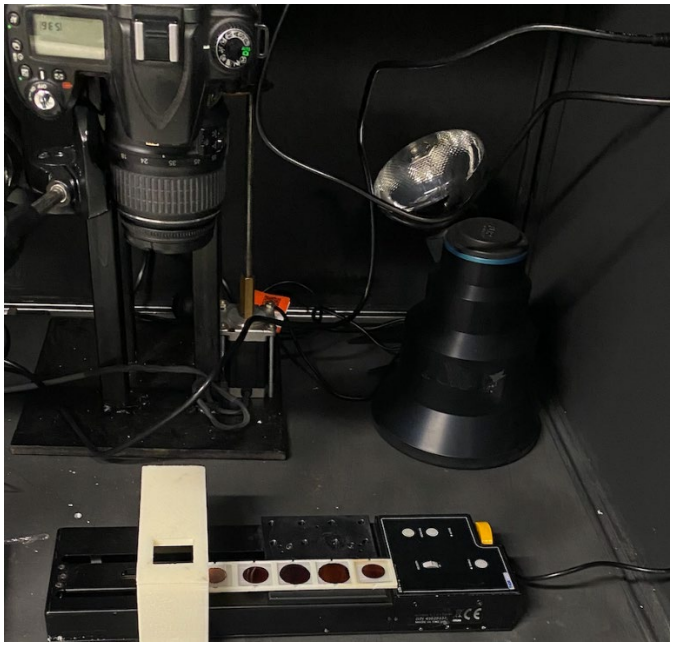

Figure S9. Images.

Optical properties

Transmission and reflection spectra were obtained on a Perkin Elmer Lambda 1050 UV-Vis-NIR spectrophotometer equipped with an integrating sphere (150 mm InGaAs Integrating Sphere) relative to a standard of known reflectivity. These two measurements were then used to calculate the absorptance (A) according to the equation A = 100 − (R + T). Photographs

were taken using a Canon EOS 450 D with an EFS 60 macro lens. Time-resolved photoluminescence spectroscopy (TRPL) samples were measured using identical excitation conditions (at excitation source wavelength = 466 nm) using a low-intensity pulse diode laser (500 kHz). The step size was set to 1 nm.

Photoelectron spectroscopy in air (PESA)

The measurements were performed using a Riken Keiki AC-2 spectrometer. For all samples, a power intensity of 20 nW was used.

Surface morphology

Scanning Electron Microscopy: Scanning electron microscopy images of the thin film surface and cross-sections of the PSCs were recorded on a FEI Magellan 400 FEG microscope using a 3 kV acceleration voltage.

Atomic Force Microscopy: AFM measurements were performed on a Dimension Icon (Veeco) in air. Chromium-platinum-coated conductive probes (ElectriMulti75-G, BudgetSensors) were used for the measurements. The scanning area and scanning rate were 50 × 50 μm and 0.5 Hz, respectively. Grain cluster size was fitted by Gwyddion software. Grain boundaries were marked using 'Mark by Segmentation' function and the grain size was calculated automatically.

Voc (reverse scan) [V]	Jsc (reverse scan) [mA/cm2]	FF (reverse scan) %	PCE (reverse scan) [%]	Device
0.105	2.46	25.20	0.15	1
0.532	20.96	35.60	3.95	2
0.718	13.58	49.50	7.29	3
0.244	4.26	25.50	0.33	4
0.728	20.00	52.20	10.59	5
0.249	16.40	39.80	6.18	6
0.072	0	0.00	0	7
0.975	11.27	53.80	5.96	8
0.684	12.56	55.60	6.82	9
1.016	13.51	57.30	7.87	10
1.008	12.78	56.30	7.25	11
0.836	7.48	49.90	4.07	12
0.999	12.22	56.30	6.86	13
1.004	9.71	55.80	5.44	14
0.923	8.18	53.90	4.32	15
0.955	13.25	50.5	6.34	16
0.819	8.68	51.5	4.84	17
0.987	9.91	57.7	5.65	18
0.898	15.02	31.9	4.15	19
0.532	20.43	29.5	4.49	20
0.49	4.72	29.7	0.4	21
0.058	4.57	23.2	0.19	22
0.235	5.67	24.2	0.1	23
0.521	13.2	29.5	2.38	24
0.089	1.81	24.8	0.05	25
0.226	5.67	25	0.51	26
0.931	17.57	36.2	5.73	27
0.033	0.48	24.4	0	28
0.267	1.88	25	0.13	29
0.848	12.94	32.9	3.57	30
0.417	3.78	25.4	0.41	31
0.134	0.94	24.9	0.04	32
0.029	0.87	24.4	0.01	33
0.094	1.07	24.9	0.03	34
0.087	0.88	24.9	0.02	35
0.043	0	0	0	36
0.136	1.23	25.2	0.04	37
0.44	4.36	25.8	0.52	38
0	0	0	0	39
0.303	14.59	32.4	3.38	40
0.104	1.41	25.1	0.04	41
0.002	0	0	0	42
1.009	17.29	53.8	9.37	43
0.298	13.5	26.1	1.37	44
0.854	7.89	49.6	4.53	45
0.17	11.06	42.1	4.72	46
1.021	16.7	51.7	8.81	47
0.988	11.87	58.6	7.12	48
0.548	12.32	49	6.23	49
1.041	13.07	56.3	7.71	50
0.781	12.74	26.7	2.77	51
0.671	13	35	3.97	52
1.027	23.12	55.1	13.09	53
0.825	4.05	31.8	1.19	54
0.65	9.38	26.3	1.67	55
1.049	25.42	34.1	8.76	56
0.981	14.09	59.1	8.24	57
0.004	0	0	0	58
0.518	18.91	31.8	4.84	59
0.817	7.02	55.7	3.82	60
0.008	0	0	0	61
0.174	9.97	27.5	1.35	62
1.056	15.77	56	9.35	63
1.034	15.6	59.8	9.7	64
0.871	23.29	32.5	8	65
0.785	8.86	43.3	3.55	66
1.014	12.28	54.7	6.84	67
0.97	14.54	54.8	7.69	68
0.627	10.92	55.9	6.04	69
0.966	13.12	59.5	7.6	70
0.835	11.33	46.4	5.74	71
0.179	1.61	25.1	0.08	72
0	0	0	0	73
0.692	13.42	57	7.77	74
0.231	16.25	34	4.38	75
0.327	3.65	25.2	0.32	76
0.674	14.68	29.1	3.6	77
0.579	14.65	30.1	3.2	78
0.91	10.2	27.4	2.51	79
1.077	10.56	29.7	3.32	80
0.06	0.93	24.8	0.01	81
0.541	16.27	29.1	2.33	82
0.992	13.65	57.4	7.81	83
0.62	16.74	28.7	3.24	84
0.81	7.22	28.2	1.71	85
1.035	14.62	55.9	8.49	86
0.991	12.4	48	5.91	87
0.043	0.65	24.3	0.01	88
0.505	6.12	25.3	0.79	89
0.371	3.59	28.1	0.47	90
0.87	8.58	29.2	2.15	91
0.578	6.91	25.6	1.05	92
0.295	3.49	25.6	0.27	93
0.304	3.08	25.2	0.26	94
0.332	2.48	25.3	0.21	95
0.245	3.48	23.1	0.2	96
0.03	0	0	0	97
0.03	0	0	0	98
0.856	20.27	49.6	8.57	99
0.991	12.4	48	5.91	100

Figure S10. Performance of the initial 100 solar cells fabricated.

Supporting References

1. SURMIAK, M. A. High-Throughput Perovskite Solar Cell Materials Discovery. Monash University, 2021.